

The influence of manganese content on the stacking fault and austenite/ ϵ -martensite interfacial energies in Fe–Mn–(Al–Si) steels investigated by experiment and theory

D.T. Pierce^{a,b,*}, J.A. Jiménez^c, J. Bentley^d, D. Raabe^e, C. Oskay^a, J.E. Wittig^a

^a Vanderbilt University, PMB 351683, 2301 Vanderbilt Place, Nashville, TN 37232, USA

^b Advanced Steel Processing and Products Research Center, Colorado School of Mines, Golden, CO 80401, USA

^c Centro Nacional de Investigaciones Metalúrgicas (CSIC), Avda. Gregorio del Amo, 8, 28040 Madrid, Spain

^d Microscopy and Microanalytical Sciences, P.O. Box 7103, Oak Ridge, TN 37831-7103, USA

^e Max-Planck-Institut für Eisenforschung, Max-Planck Str. 1, D-40237 Düsseldorf, Germany

Received 20 September 2013; received in revised form 1 January 2014; accepted 1 January 2014

Abstract

The stacking fault and interfacial energies of three transformation- and twinning-induced plasticity steels (TRIP/TWIP) (Fe–22/25/28Mn–3Al–3Si wt.%) were determined by experimental and theoretical methods. Analysis of Shockley partial dislocation configurations in the three alloys using weak-beam dark-field transmission electron microscopy yielded stacking fault energy (SFE) values of 15 ± 3 , 21 ± 3 and 39 ± 5 mJ m^{-2} for alloys with 22, 25 and 28 wt.% Mn, respectively. The experimental SFE includes a coherency strain energy of $\sim 1\text{--}4$ mJ m^{-2} , determined by X-ray diffraction, which arises from the contraction in volume of the stacking fault upon the face-centered cubic (fcc) to hexagonal close-packed (hcp) phase transformation. The ideal SFE, computed as the difference between the experimental SFE and the coherency strain energy, is equal to 14 ± 3 , 19 ± 3 and 35 ± 5 mJ m^{-2} , respectively. These SFE values were used in conjunction with a thermodynamic model developed in the present work to calculate the free energy difference of the fcc and hcp phases and to determine a probable range for the fcc/hcp interfacial energy in the three Fe–Mn–(Al–Si) steels investigated. In addition, the interfacial energies of three Fe–18Mn–0.6C–0/1.5(Al/Si) TWIP and five Fe–16/18/20/22/25Mn binary alloys were also determined from experimental data in the literature. The interfacial energy ranged from 8 to 12 mJ m^{-2} in the TRIP/TWIP steels and from 15 to 33 mJ m^{-2} in the binary Fe–Mn alloys. The interfacial energy exhibits a strong dependence on the difference in Gibbs energy of the individual fcc and hcp phases. Accordingly, an empirical description of this parameter is proposed to improve the accuracy of thermodynamic SFE calculations.

© 2014 Acta Materialia Inc. Published by Elsevier Ltd. All rights reserved.

Keywords: TWIP steel; Phase stability; Partial dislocation; Stacking fault energy; Interface energy

1. Introduction

High-manganese austenitic transformation- and twinning-induced plasticity (TRIP/TWIP) steels are a superior class of materials that exhibit excellent strain hardening, strength, ductility and toughness [1–8]. This combination

of mechanical properties is attractive for automotive applications requiring high room-temperature formability and weight reduction. These alloys typically include $\sim 18\text{--}30$ wt.% Mn and additions of Al, Si, Cr, C and N with microstructures of meta-stable or stable austenite [9–12]. During straining, the austenite deforms by dislocation glide together with secondary deformation mechanisms, including $\alpha_{\text{bcc}}/\epsilon_{\text{hcp}}$ -martensite formation and/or mechanical twinning [13]. The martensite platelets and mechanical twins act

* Corresponding author. Tel.: +1 8602873437; fax: +1 6153436614.
E-mail address: dean.t.pierce@vanderbilt.edu (D.T. Pierce).

as planar obstacles and reduce the mean free path of dislocation glide. As deformation progresses, these strain-induced features increasingly refine the grain structure, causing a dynamic Hall–Petch effect [5,14–22]. The result is high strain hardening, delayed necking and large uniform elongations [1]. A separate theory attributes the strain hardening in high-Mn steels containing a significant C content to dynamic strain aging (DSA) and not mechanical twinning [23]; however, more recent reports [22] conclude that DSA plays only small role in the hardening compared to mechanical twinning.

The low stacking fault energy (SFE) of these steels allows for secondary deformation mechanisms (the TRIP/TWIP effect). With decreasing SFE, the plasticity mechanisms change from (i) dislocation glide to (ii) dislocation glide and mechanical twinning to (iii) dislocation glide and $\gamma_{fcc} \rightarrow \epsilon_{hcp}$ martensitic transformations [3,24–28]. Each deformation mode results in different mechanical properties. Consequently, designing TRIP/TWIP alloys requires a reliable method of predicting SFE.

Many studies correlate microstructural observations of deformation mechanisms and mechanical properties with thermodynamic calculations of the SFE. The method proposed by Olson and Cohen [29], and adapted by several other authors [3,12,25,27], treats the fault as n layers of hexagonal close-packed (hcp) phase separated from the face-centered cubic (fcc) matrix by two interfaces. The SFE can be calculated as:

$$\gamma_{\infty} = n\rho(\Delta G_{Chem}^{fcc \rightarrow hcp} + \Delta G_{Mag}^{fcc \rightarrow hcp}) + 2\sigma^{\gamma/\epsilon} \quad (1)$$

where γ_{∞} is the ideal SFE (mJ m^{-2}) of the fault (unbounded by partial dislocations), n is equal to 2 for an intrinsic stacking fault, and $\Delta G_{Chem}^{fcc \rightarrow hcp}$ and $\Delta G_{Mag}^{fcc \rightarrow hcp}$ (mJ mol^{-1}) are the chemical and magnetic contributions, respectively, to the difference in Gibbs free energy of the fcc and hcp phases. The term $\Delta G_{Mag}^{fcc \rightarrow hcp}$ arises from antiferromagnetic ordering. With decreasing temperature both the fcc and hcp phases in Fe–Mn-based alloys undergo a paramagnetic to antiferromagnetic state change at their respective Néel temperatures [3,4,12,18,25–27]. Antiferromagnetic ordering has a stabilizing influence and lowers the Gibbs free energy of the individual phases. The term $\sigma^{\gamma/\epsilon}$ (mJ m^{-2}) is the interfacial energy between the fcc phase and the hcp phase, and ρ is the molar surface density (mol m^{-2}) of $\{111\}$, defined as:

$$\rho = \frac{4}{\sqrt{3}a_{fcc}^2} \frac{1}{N_A} \quad (2)$$

The term N_A is Avogadro's number and a_{fcc} is the lattice parameter of the fcc phase. Allain et al. [25] studied an Fe–22Mn–0.6C wt.% steel and concluded that ϵ_{hcp} -martensite formation occurs for calculated SFEs below 18 mJ m^{-2} while mechanical twinning is active from 12 to 35 mJ m^{-2} . Thermodynamic SFE calculations by Saeed-Akbari et al. [27] indicate an upper limit of 20 mJ m^{-2} for strain-induced ϵ_{hcp} -martensite transformation. Nakano

and Jacques [30] calculated SFE values for the Fe–Mn and Fe–Mn–C systems and correlated these with microstructural observations from other investigators, finding strain-induced ϵ_{hcp} -martensite to occur at SFEs as high as 41 mJ m^{-2} . In the literature, the lack of agreement between the SFE value and deformation mechanisms results from different thermodynamic parameters and interfacial energies, with $\sigma^{\gamma/\epsilon}$ varying from 9 mJ m^{-2} [25] to 16 mJ m^{-2} [30]. Saeed-Akbari et al. [27] utilized a value of 15 mJ m^{-2} , but acknowledged the uncertainty of this parameter in Fe–Mn-based alloys, citing literature values that ranged from 5 to 27 mJ m^{-2} .

The uncertainty of the interfacial parameter in Fe–Mn-based systems limits the effectiveness of thermodynamic SFE models. Olson and Cohen [29] proposed to indirectly calculate $\sigma^{\gamma/\epsilon}$ using experimental SFE values, γ_{exp} . The term γ_{exp} also includes a coherency strain energy, E_{str} (J mol^{-1}), arising from the contraction in molar volume of the hcp stacking fault relative to the fcc matrix (note: the same coherency strain energy is typically not accounted for in thermodynamic SFE values). The strain energy must be subtracted from the experimental SFE value as in Eq. (3):

$$\gamma_{\infty} = \gamma_{exp} - n\rho E_{str} \quad (3)$$

to yield γ_{∞} . Combining Eqs. (1) and (3) gives:

$$\sigma^{\gamma/\epsilon} = \frac{1}{2}(\gamma_{exp} - n\rho(E_{str} + \Delta G_{Chem}^{fcc \rightarrow hcp} + \Delta G_{Mag}^{fcc \rightarrow hcp})) \quad (4)$$

Cotes et al. [31] used experimental SFE values from measurements of extended dislocation nodes [32,33] to determine room temperature values of $\sigma^{\gamma/\epsilon}$, ranging from 16 to 26 mJ m^{-2} , for binary Fe–Mn alloys. However, by comparison to SFE measurements from Shockley partial dislocation pairs, measurements from extended dislocation nodes are usually higher and result in greater uncertainty [34,35]. Heat treatments were typically required to form symmetrical nodes in Fe–Cr–Ni specimens [34]. In that study, the authors found the room-temperature node size to vary inversely with prior heat treatment temperature, suggesting that the nodes were inhibited from returning to the equilibrium configuration after heating. Since the effect was not observed on the separation of partial dislocation pairs, the authors suggested that nodes were more susceptible to solute impedance forces, which resulted in higher apparent SFE measurements. However, the general trend in SFE values for different grades of austenitic stainless steel was similar for each method of measurement. In a study by the present authors [35], the formation of nodes in Fe–Mn–Al–Si steels required heat treatments in excess of $650 \text{ }^{\circ}\text{C}$, and then only resulted in non-isolated and mostly asymmetrical nodes unsuitable for measurement. Therefore, the SFE values reported for binary Fe–Mn alloys [32,33] may overestimate the true values. Consequently, the interfacial energy determined from these SFE values may also be systematically overestimated.

Stacking fault energy measurements on TRIP/TWIP steels by analysis of partial dislocation pairs using

weak-beam dark-field (WBDF) transmission electron microscopy (TEM) have been reported for Fe–20Mn–1.2C ($\gamma_{exp} = 15 \text{ mJ m}^{-2}$) [36], Fe–18Mn–0.6C ($\gamma_{exp} = 13 \pm 3 \text{ mJ m}^{-2}$) [10], Fe–18Mn–0.6C–1.5Al ($\gamma_{exp} = 30 \pm 10 \text{ mJ m}^{-2}$) [10] and Fe–25Mn–3Al–3Si ($\gamma_{exp} = 16 \pm 4 \text{ mJ m}^{-2}$) [35] alloys. The following concerns arise from evaluating these studies: equilibrium partial dislocation separations are a balance between the restorative force due to the SFE and the repulsive elastic force of the partial dislocations [37]. Determination of the elastic repulsive force acting on dislocations in anisotropic materials requires the single-crystal elastic constants. The experimental studies rely on bulk elastic properties [10] and single-crystal elastic constants from other grades of steel [36] or ab initio simulations [35,38–40]. Recent work by the present authors [41] provides experimental values of single-crystal elastic constants for Fe–Mn–Al–Si and Fe–Mn–C–Al steels necessary for SFE measurements. As such, the previously reported SFE value of $16 \pm 4 \text{ mJ m}^{-2}$ for an Fe–25Mn–3Al–3Si alloy [35] will be updated in the present work by utilizing the more accurate experimental elastic constants. Secondly, in the study on the Fe–18Mn–0.6C–0/1.5Al grades [10], a distinction between the separation of two partial dislocation images and separation of the cores is not made, which can impact SFE values for small partial dislocation separations (as described in Sections 3.1 and 4.1). Finally, the effect of Mn content on the SFE cannot be understood from the three studies given the large differences in other alloying additions.

The goals of the present study are to:

1. quantify the influence of Mn content on SFE by applying the elastic constants determined in [41] to Shockley partial dislocation separations for three Fe–22/25/28Mn–3Al–3Si wt.% alloys;
2. experimentally determine E_{str} and γ_{∞} for the three Fe–22/25/28Mn–3Al–3Si alloys; and
3. calculate $\sigma^{\gamma/\epsilon}$ for the three Fe–22/25/28Mn–3Al–3Si alloys and other Fe–Mn-based alloys for which experimental SFE data exists in the literature.

The observed deformation microstructures and mechanical properties as a function of Mn content and SFE will be reported in a subsequent paper.

2. Materials

Three alloys were induction melted in an argon atmosphere and cast into ingots. The compositions are listed in Table 1. As-cast ingots were thermomechanically pro-

cessed by hot rolling at 1100 °C to produce strips of 3 mm thickness and subsequently by cold rolling to 1.5 mm thickness. The resulting sheet was recrystallized at 900 °C for 30 min in air, yielding a microstructure with equiaxed grains of $\sim 21 \mu\text{m}$ diameter for each composition. Oxide layers formed during this treatment were removed by machining. The steels with 25% and 28% Mn were fully austenitic, while the alloy with 22% Mn contained a small amount of ferrite (<1%) in the recrystallized condition. Sub-sized flat tensile specimens with a 20 mm gauge length and 5 mm width were cut from the sheet in the direction parallel to the rolling direction using electrodischarge machining (EDM).

3. Experimental procedure

Specimens of the 22%, 25% and 28% Mn alloys were strained in tension at a rate of $4 \times 10^{-4} \text{ s}^{-1}$ to the yield point (YP) and 1.5% plastic strain for SFE measurements by TEM. Thermal treatments of 650–700 °C for 48–70 h were applied to samples strained 1.5% to produce equilibrium dislocation configurations. Additional samples of the 22%, 25% and 28% Mn alloys were strained to failure at room temperature, –25 and –100 °C, respectively, in order to introduce strain-induced ϵ_{hcp} -martensite for measurement of lattice parameters. The 25% and 28% Mn alloys were deformed at lower temperatures, where enough driving force exists to transform sufficient quantities of austenite into ϵ_{hcp} -martensite. The lattice parameters of the fcc and hcp phases were measured by X-ray diffraction (XRD) at room temperature from as-recrystallized (for fcc) and deformed (for hcp) specimens.

3.1. Stacking fault energy measurements

Disks 3 mm in diameter were cut from the gauge length of deformed samples using EDM. The 3 mm disks were mechanically polished to 100 μm thickness and then jet electropolished to electron transparency with a TenuPol-5 using a solution of 70% methanol and 30% nitric acid at –30 °C. Partial dislocations were analyzed with a Philips CM20T transmission electron microscope operating at 200 kV.

Measurements of Shockley partial dislocation separations were made with a beam direction near the [1 1 1] zone on defects in the (111) habit plane using (-220) -type g -vectors. Bright-field (BF) and WBDF imaging modes were employed, with the WBDF diffracting conditions set at $g(3g)$ or $g(4g)$ and with no non-systematic reflections excited. The $g(3g)$ configuration results in a deviation parameter $s_g = 0.15 \text{ nm}^{-1}$ and $w = \xi_g s_g = 12.4$, where ξ_g

Table 1
Chemical compositions of the steels in wt.% unless otherwise specified.

Designation	Material	Mn	Al	Si	C	O (ppm)	Fe
22%Mn	Fe–22Mn–3Al–3Si	22.2	2.76	2.92	0.0093	<5	Bal.
25%Mn	Fe–25Mn–3Al–3Si	24.7	2.66	2.95	0.0053	<5	Bal.
28%Mn	Fe–28Mn–3Al–3Si	27.5	2.74	2.89	0.0071	<5	Bal.

is the extinction distance. The value of s_g in the $g(3g)$ configuration is slightly less than the recommended value of 0.2 nm^{-1} [42] and this results in slightly larger than ideal image widths. For partial dislocation separations below $\sim 4 \text{ nm}$, as in the 28% Mn alloy, the $g(4g)$ configuration ($s_g = 0.23 \text{ nm}^{-1}$, $w = \xi_g s_g = 18.5$) was utilized to improve the resolution of the partial dislocations. Measurements were made every 5–10 nm along the length of long, straight sections of isolated dislocations in areas not significantly affected by image forces and constrictions. Since the strain fields outside and between partial dislocations are asymmetrical, the intensity peaks are not equidistant from their respective dislocation cores and a correction is applied to determine the actual partial dislocation spacing, d_{actual} [43]. An average d_{actual} and standard deviation of the measurements were obtained for each partial dislocation pair. Inside–outside contrast techniques (reversing the \mathbf{g} -vector) were additionally applied to differentiate partial dislocations from dipoles. The total dislocation character angle, β , was determined from Burgers vector analysis on the partial dislocations in WBDF imaging mode. For Shockley partial dislocations in the $[111]/(111)$ zone/habit plane configuration, $|\mathbf{g} \cdot \mathbf{b}_p|$ (where \mathbf{b}_p is the partial dislocation Burgers vector) values are 1 or 0 and $|\mathbf{g} \cdot \mathbf{b}_p| = 1$ for both partials at only one \mathbf{g} -vector. When the latter condition is achieved, the total Burgers vector is parallel to the \mathbf{g} -vector, and the angle it makes with the dislocation line vector is the total dislocation character angle. The habit plane was confirmed by stereographic analysis from BF images of the dislocations taken at three different locations.

3.2. X-ray diffraction

Measurements of lattice parameters utilized a Bruker AXS D8 diffractometer equipped with a Co X-ray tube, Goebel mirror optics and a LynxEye Linear Position Sensitive Detector for ultrafast XRD measurements. A current of 30 mA and a voltage of 40 kV were employed as tube settings. Operational conditions were selected to obtain XRD profiles of sufficient quality: namely, optimal counting statistics, narrow peaks and detection of small diffraction peaks of minor phases. The XRD data were collected over a 2θ range of $30\text{--}120^\circ$, with a step size of 0.02° .

For the application of the Rietveld refinement, instrument functions were empirically parameterized from the profile shape analysis measured under the same conditions for an AISI Type 316 stainless steel standard prepared by hot isostatic pressing. In this study, version 4.2 of the Rietveld analysis program TOPAS (Bruker AXS) was used for the XRD data refinement. The refinement protocol included the background, zero displacement, scale factors, peak width, unit cell parameters and texture parameters. The room-temperature structures used in the refinement were ferrite, austenite and ϵ_{hcp} -iron. The quality and reliability of the Rietveld analysis was quantified by the corresponding figures of merit: the weighted summation of the

residual of the least-squares fit, R_{wp} , the statistically expected least-squares fit, R_{exp} , the profile residual, R_p , and the goodness of fit (sometimes referred to as chi-squared), GoF. Since $\text{GoF} = R_{wp}/R_{exp}$, a GoF of 1.0 means a perfect fitting.

4. Results and discussion

4.1. SFE measurements

Additions of Mn from 22 to 28 wt.% increase the SFE and reduce the partial dislocation separations. Partial

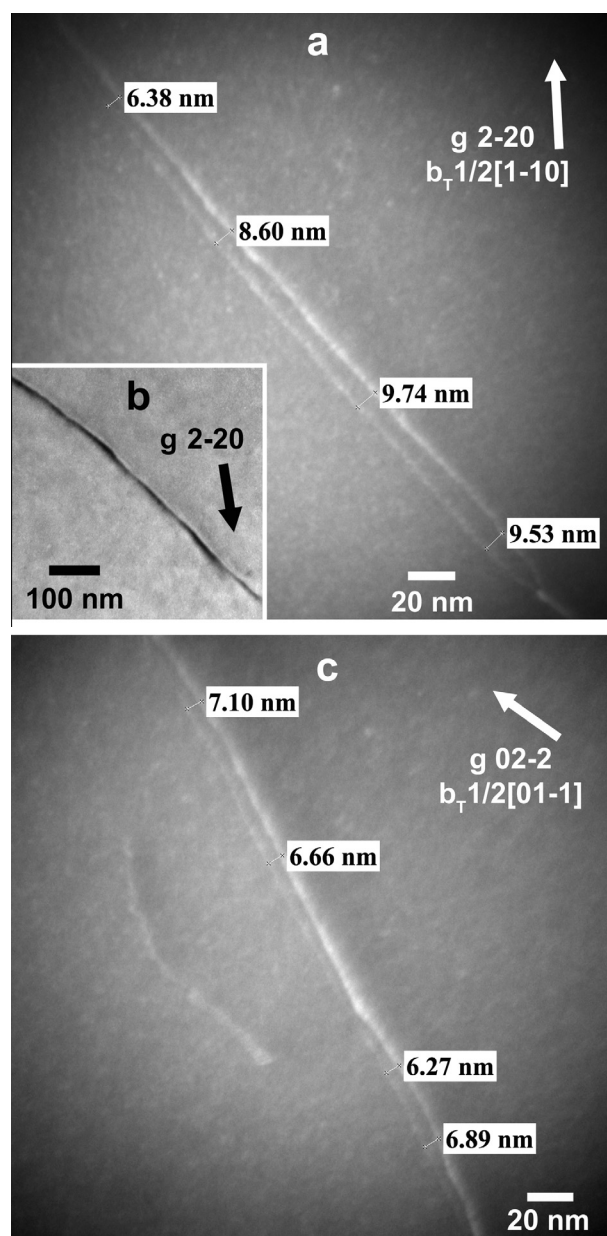


Fig. 1. Images of dislocations in 22% Mn specimens deformed to the YP. (a) WBDF and (b) corresponding BF image of a partial dislocation pair. (c) WBDF image of a second partial dislocation pair closer to screw character and displaying reduced separation. Only a few representative separation measurements are shown.

dislocation core separations in the 22% Mn alloy ranged from 6 to 13 nm, depending on the character angle. Fig. 1a displays a WBDF image of a partial dislocation pair with a character angle of 39° in a specimen deformed to the YP. The average actual partial dislocation core separation is 9.3 ± 1.1 nm, in which the uncertainty is one standard deviation of all measurements along the length of the dislocation (note: measurements were taken every 5–10 nm along the length of dislocations but most have been removed from the figures for clarity). The BF image in Fig. 1b of the same dislocation illustrates the increased resolution of the WBDF technique. In Fig. 1c, a dislocation pair in a 22% Mn specimen deformed to the YP with a smaller character angle of 26° exhibits an average core separation of 6.6 ± 0.5 nm. Due to a low SFE, partial dislocation separations in the 22% Mn alloy displayed greater variations and susceptibility to image forces, as evidenced by partial dislocations in specimens deformed to the YP in Fig. 2. The width of the partials in Fig. 2a fluctuates dramatically at the foil surfaces, where the partials are constricted at one intersection while showing a large separation distance at the other. In Fig. 2b, a partial dislocation pair in the (111) habit plane normal to the [111] beam, imaged with a $-220\mathbf{g}$ -vector, is interacting with a stacking fault on (-111) . The partial dislocations in (111) experience a contraction in their separation at the intersection with the partial dislocation on the inclined plane. In an image of the same defects with a $02-2\mathbf{g}$ -vector (Fig. 2c), one of the partials on (111) ($|\mathbf{g}\cdot\mathbf{b}_p|=0$) and SF on (-111) become invisible. This study avoided

partial dislocations such as those in Fig. 2 for quantitative measurements.

The separation of partials in the 25% Mn alloy ranged from 4 to 7 nm, with Fig. 3 showing a partial dislocation pair with average actual spacing of 4.9 ± 0.5 nm and a total character angle of 22° . The present authors reported additional measurements of dislocations from this alloy in [35].

Partial dislocation separations in the 28% Mn alloy ranged from 2.6 to 4.3 nm. Imaging with $g(4\mathbf{g})$ diffracting conditions decreased image-widths and reduced the discrepancy between observed and actual partial dislocation separations. In Fig. 4a, a partial dislocation pair with kinks or jogs along its length and a character angle of 40° exhibits an average actual spacing of 3.3 nm on uniform sections. In Fig. 4b, a partial dislocation pair with a character angle of 15° displays an average actual spacing of 2.5 nm. At small spacing, the intensity peak generated from between the partial dislocations becomes significantly weaker due to fewer atomic planes oriented for scattering, as clearly shown in Fig. 4b [44].

The character of stacking faults (intrinsic vs. extrinsic) in the present alloys, as determined by typical diffraction contrast methods (e.g. [44,45]), is intrinsic. Fig. 5a–c displays three dark-field TEM micrographs of stacking faults corresponding to the 22%, 25% and 28% Mn alloys, respectively. Of ~ 10 faults investigated for each alloy, all were intrinsic.

Fig. 6 displays the average spacing of partial dislocation pairs in the three alloys. Theoretical partial dislocation spacing curves based on Eq. (5), formulated by Aerts et al. [46], are fitted to the experimental data to determine the SFE. The relationship is an excellent approximation of

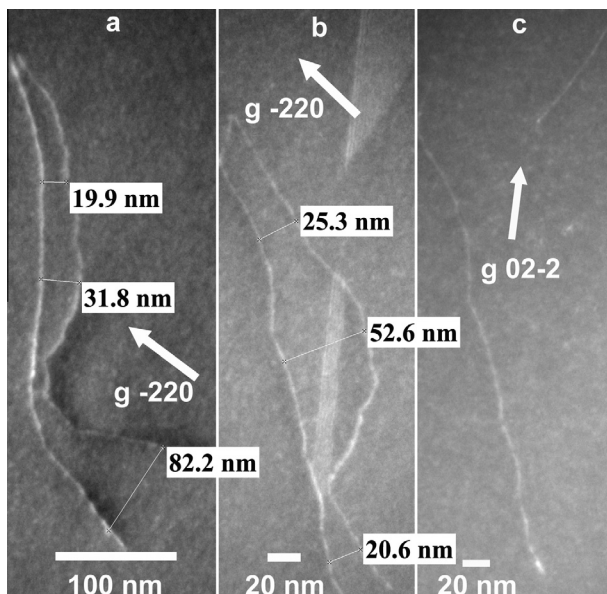


Fig. 2. WBDF images of partial dislocation pairs in a 22% Mn alloy deformed to the YP. In (a) the partials display non-uniform separation, most dramatically at the intersections with the foil surfaces. In (b) a partial dislocation pair residing in (111) normal to the [111] beam direction is interacting with a stacking fault on (-111) . In (c), the defects in (b) are imaged with a $02-2$ diffracting vector, leading to invisibility of one of the partials in (111) and the SF on (-111) .

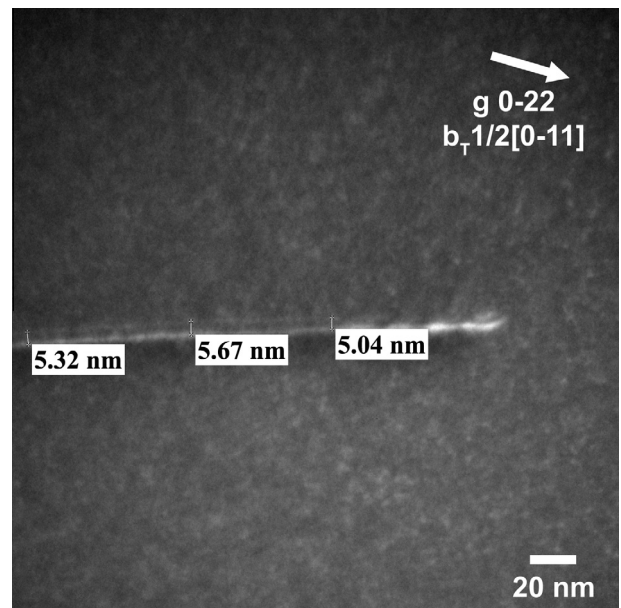


Fig. 3. A WBDF image of a partial dislocation pair in an Fe-25Mn-3Al-3Si alloy deformed to the YP.

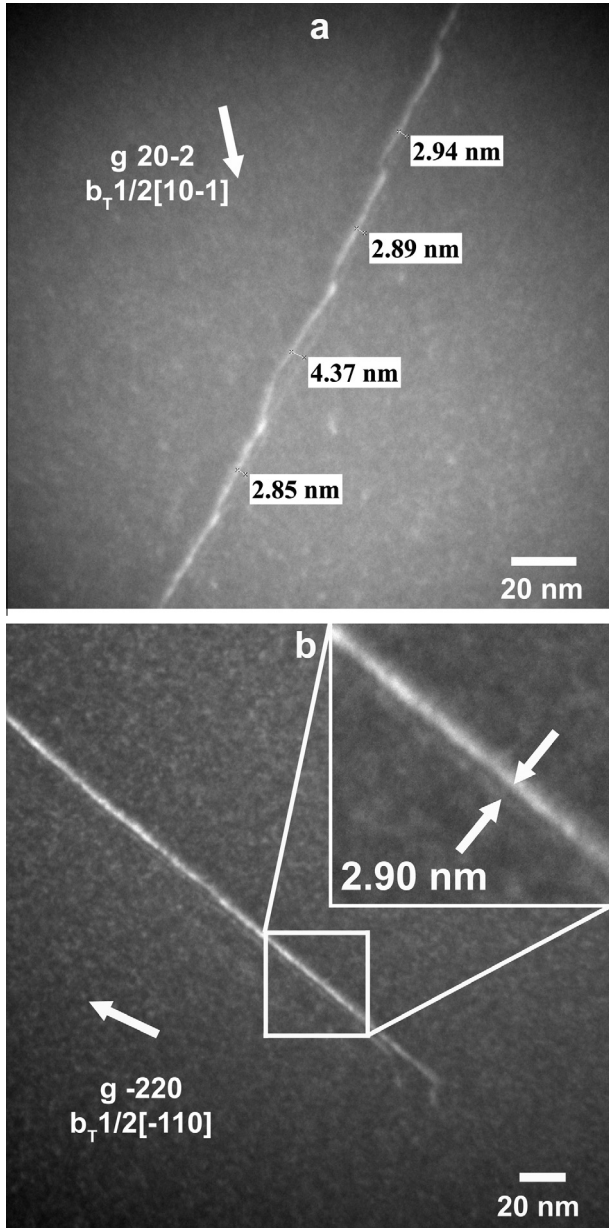


Fig. 4. WBDF images of partial dislocation pairs in specimens of the 28% Mn alloy deformed to (a) the YP and (b) 1.5% with heat treatment of 650 °C for 48 h.

anisotropic theory, as shown by Teutonico [47], and avoids the significant complexity of pure anisotropic dislocation theory [48–50], in which solutions are available only for specific dislocation configurations.

$$d_{actual} = \frac{\mu_{eff} b_p^2}{8\pi\gamma_{exp}} \frac{2 - \nu_{eff}}{1 - \nu_{eff}} \left(1 - \frac{2\nu_{eff} \cos 2\beta}{2 - \nu_{eff}} \right) \quad (5)$$

The term b_p is the $a_o/6 \langle 112 \rangle$ partial dislocation Burgers vector, determined by XRD of recrystallized Fe–22/25/28Mn–3Al–3Si specimens to be 0.1476, 0.1477 and 0.1479 nm, respectively, and the total dislocation character angle is β . The effective shear modulus, μ_{eff} , for dislocations in $\{111\}$ is a function of the single-crystal elastic stiffness constants C_{11} , C_{12} and C_{44} , and is defined by Eq. (6):

$$\mu_{eff} = \left(C_{44} \frac{(C_{11} - C_{12})}{2} \right)^{0.5} \quad (6)$$

Eqs. (7) and (8) denote the relationship between the effective Poisson's ratio, ν_{eff} , and the single-crystal elastic constants:

$$\frac{1}{1 - \nu_{eff}} = \frac{1}{3\mu_{eff}} (C + C_{12}) \left[\frac{C_{44}(C - C_{12})}{C_{11}(C + C_{12} + 2C_{44})} \right]^{0.5} \left(1 + 2\frac{C_{11}}{C} \right) \quad (7)$$

$$C = \left[\frac{1}{2} C_{11}(C_{11} + C_{12} + 2C_{44}) \right]^{0.5} \quad (8)$$

For the 22%, 25% and 28% Mn alloys, $\mu_{eff} = 67 \pm 4$, 66 ± 4 , 66 ± 4 GPa and $\nu_{eff} = 0.30$, 0.31 and 0.31, respectively. The terms μ_{eff} and ν_{eff} account for anisotropic elasticity in $\{111\}$, and are calculated from Eqs. (6)–(8) using single-crystal elastic constants determined by the present authors [41]. The experimental SFEs for the 22%, 25% and 28% Mn alloys are 15 ± 3 , 21 ± 3 and 40 ± 5 mJ m⁻², respectively. The large increase in SFE energy above 25 wt.% Mn is consistent with experimental SFE measurements by Volosevich et al. [32] and observations that show a sharp reduction in the ϵ_{hcp} -martensite start temperature for additions of Mn above 25 wt.% in binary Fe–Mn alloys [30,31]. The uncertainty of the SFE is primarily due to the scatter of average d_{actual} values between different dislocations (data points in Fig. 6) and uncertainties of ν_{eff} and μ_{eff} . The first two sources of uncertainty are accounted for by fitting upper and lower bounds (SFE curves) that encompass the majority of the data points for a given composition as shown in Fig. 6. The uncertainty from these two sources was determined to be ± 20.0 , ± 14.3 and $\pm 12.5\%$ of the SFE for the 22%, 25% and 28% Mn alloys, respectively. The uncertainty of μ_{eff} is $\pm 6.0\%$. The final uncertainty of the SFE for the 22%, 25% and 28% Mn alloys was obtained from the root sum square of the two calculated values and is ± 20.9 (e.g. $(20.0^2 + 6.0^2)^{0.5}$), ± 15.5 and $\pm 13.9\%$ or ± 3 , ± 3 and ± 5 mJ m⁻² (rounded to one significant figure). Volosevich et al. [32] reported SFE values of ~ 15 and 27.5 mJ m⁻² for Fe–22/25Mn wt.% alloys, respectively, by TEM observation of extended nodes. These values likely overestimate the SFE, since the combined effect of adding 3 wt.% Al and Si would raise the SFE, yet the SFE values of the Fe–22/25Mn–3Al–3Si steels are equal or less. If isotropic elasticity is applied to the present measurements on the 22% Mn alloy, by replacing the effective elastic constants in Eq. (5) with a polycrystalline shear modulus (72 GPa) and Poisson's ratio (0.24) [41], the SFE is 16 ± 4 mJ m⁻² (dashed lines in Fig. 6). The SFE determined with isotropic elastic constants overestimates the anisotropic value by $\sim 7\%$ and results in a poorer data fit, producing a larger uncertainty of ± 4 mJ m⁻². The overestimation of the SFE results from the use of the larger isotropic shear modulus and the poorer data fit stem from the large difference between the isotropic and effective values of the Poisson's

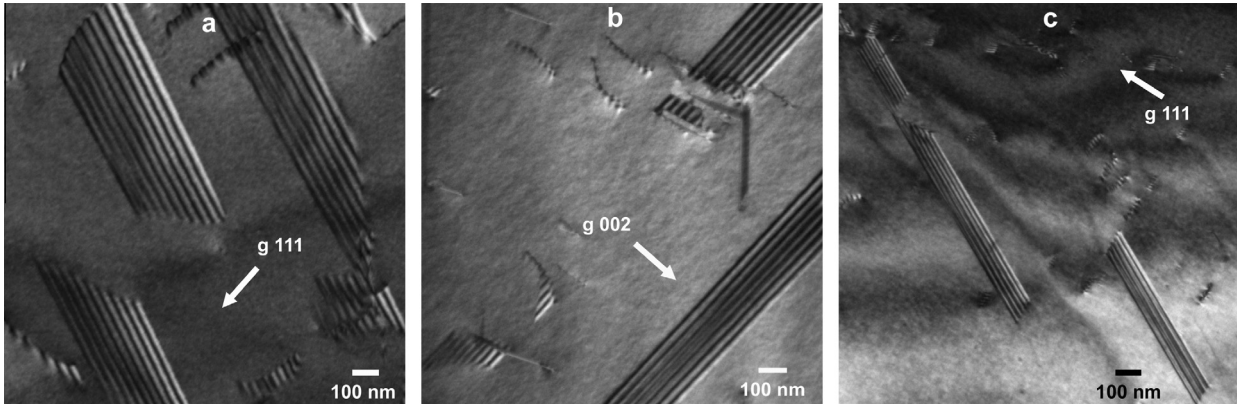


Fig. 5. Dark-field images of intrinsic SFs in (a) the 22% Mn, (b) the 25% Mn and (c) the 28% Mn alloys as identified by the procedures in Refs. [44,45].

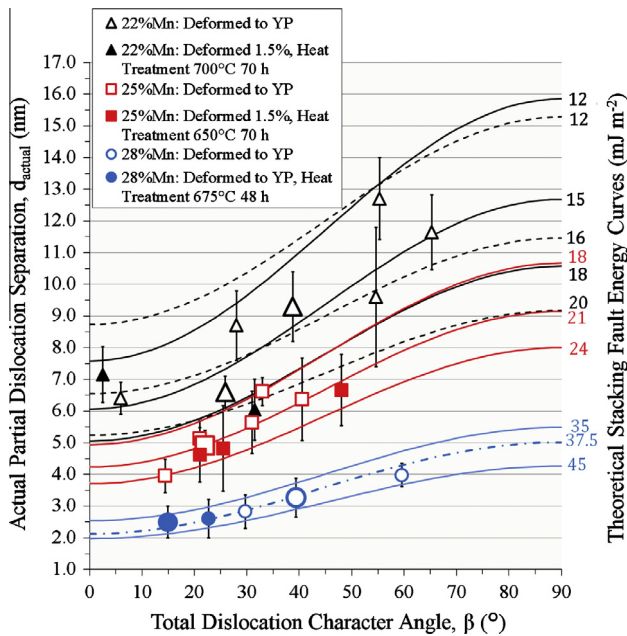


Fig. 6. Average actual partial dislocation separations for the 22%, 25% and 28% Mn alloys for specimens deformed to the YP and 1.5% with heat treatments. The error bars represent the standard deviation of the measurements on individual pairs. The dashed and solid curves represent theoretical partial dislocation spacings based on isotropic and anisotropic elasticity, respectively. The dashed-dotted line for the 28% Mn alloy assumes a Peierls core model. The larger symbols correspond to the partial dislocations from Figs. 1, 3 and 4.

ratio. The elastic anisotropy ratio ($2C_{44}/(C_{11} - C_{12})$) of the present materials is ~ 2.2 [41]. For fcc materials, μ_{eff} and ν_{eff} will become increasingly smaller and larger, respectively, relative to the polycrystalline values, as the elastic anisotropy ratio increases [47].

In the above analysis, the partial dislocation cores are treated as purely elastic defects, i.e. as singular Volterra type dislocations with a core width of zero. However, the core width of dislocations may not be zero and, at small partial dislocation separations, such as those observed in the 28% Mn alloy, core effects can influence SFE measurements, as shown by Cockayne and Vitek [51]. The dislocation core thickness can influence the force acting between

two partial dislocations and, thus, their separation. The partial dislocation separation obtained from a Peierls-type core model, $d_{Peierls}$, which accounts for core width, is related to the partial dislocation separation of Eq. (5), d_{actual} , by Eq. (9) [51]:

$$d_{Peierls} = \frac{1}{2} \left(d_{actual} + \sqrt{d_{actual}^2 - 4\zeta^2} \right) \quad (9)$$

In this model, as the core width increases, the repulsive force acting between the two partial dislocations decreases. Since the core width, ζ , is unknown, a reasonable approximation is twice the lattice parameter (0.724 nm), as employed by Cockayne and Vitek [51]. Applying this model to the partial dislocation separation measurements of the 28% Mn alloy yields an SFE of 37.5 mJ m^{-2} , as depicted in Fig. 6 (dashed-dotted line), which is slightly smaller than the 40 mJ m^{-2} obtained assuming singular cores. The fit of Eq. (9) to the partial dislocation separation measurements of the 28% Mn alloy becomes increasingly worse as the core thickness is increased above 0.724 nm. Therefore, the true value of the partial dislocation core width for the 28% Mn alloy is likely to be between 0 and 0.724 nm. As such, the SFE of the 28% Mn alloy is taken as the average of the two SFE values, $38.8 \pm 5 \text{ mJ m}^{-2}$. Since the partial dislocation separations of the 22% and 25% Mn alloys are substantially larger, assuming a core width of 0.724 nm in these alloys produced no significant change in the SFE. Cockayne and Vitek [51] also suggested that partial dislocation core widths greater than twice the lattice constant may lead to a less well defined image peak and an additional narrow image peak under certain circumstances [51]. The present authors did not observe any of these features in the WBDF images that could be attributed to core effects, giving further confidence that the partial dislocation core thickness is below 0.724 nm.

4.2. Coherency strain energy contribution

The fcc matrix and ϵ_{hcp} -martensite have the $(111)_\gamma \parallel (0001)_\epsilon / [1-10]_\gamma \parallel [1-210]_\epsilon$ orientation relationship. However, the ϵ_{hcp} -martensite phase displays a slightly

smaller molar volume than the austenite phase. Brooks et al. [52] showed the local close-packed plane (cpp) spacing of single stacking faults contracts $\sim 2\%$ relative to the cpp spacing of the austenitic matrix in Fe–Cr–Ni steels, and thus that stacking faults are ε_{hcp} -martensite embryos or nuclei. Marinelli et al. [53,54] observed decreases in the molar volume of the ε_{hcp} -martensite structure of $\sim 2\%$ relative to austenite in binary Fe–Mn alloys. The propensity to contract is resisted by the matrix (i.e. austenite phase), which results in the deformation of both austenite matrix and the martensite phase. This coherency strain increases the energy of the stacking fault complex. It is desirable to remove the coherency strain-induced energy contribution from the SFE of experimental measurements so that comparison to theoretical SFE values is applicable. The molar volumes of the fcc and hcp phases are defined in Eqs. (10) and (11), respectively, as:

$$V_{m,\text{fcc}} = \frac{a_{\text{fcc}}^3}{4} N_A \quad (10)$$

and

$$V_{m,\text{hcp}} = \frac{\sqrt{3}}{4} a_{\text{hcp}}^2 c_{\text{hcp}} N_A \quad (11)$$

where a_{fcc} , a_{hcp} and c_{hcp} are the lattice parameters of the fcc and hcp phases. The volumetric strain (VS) due to volume change from fcc to hcp phase is defined as:

$$VS = \frac{V_{m,\text{hcp}} - V_{m,\text{fcc}}}{V_{m,\text{fcc}}} \quad (12)$$

The strain (ε_{33}) corresponding to the contraction normal to the close-packed planes of the hcp structure relative to the fcc matrix is defined as:

$$\varepsilon_{33} = (c_{\text{hcp}} - c_{\text{fcc}}) / c_{\text{fcc}} \quad (13)$$

The terms c_{fcc} and c_{hcp} are twice the cpp spacing in the fcc and hcp structures, respectively. The strain terms ε_{11} and ε_{22} correspond to the contraction along $\langle 1-210 \rangle$ relative to $\langle 1-10 \rangle$ (close-packed directions) and $\langle 1-100 \rangle$ relative to $\langle 11-2 \rangle$, respectively, and are calculated similarly to ε_{33} (Eq. (13)) as a function of the lattice parameters. Several authors have investigated the energy contribution of the coherency strain, E_{str} , on SFE measurements (e.g. [29,31,55]). Olson and Cohen [29] considered the strain energy term to be the sum of the dilatation energy, E_{dil} , and the shear energy, E_{sh} :

$$E_{\text{str}} = E_{\text{dil}} + E_{\text{sh}} \quad (14)$$

where

$$E_{\text{dil}} = \frac{2(1+\nu)}{9(1-\nu)} \mu V_{m,\text{fcc}} (VS)^2 \quad (15)$$

and

$$E_{\text{sh}} = \eta V_{m,\text{fcc}} 2\mu \left\{ \frac{1}{6} \left[(\varepsilon_{11} - \varepsilon_{22})^2 + (\varepsilon_{22} - \varepsilon_{33})^2 + (\varepsilon_{33} - \varepsilon_{11})^2 \right] + \varepsilon_{12}^2 + \varepsilon_{23}^2 + \varepsilon_{13}^2 \right\} \quad (16)$$

The terms ν and μ represent the austenite phase polycrystalline Poisson's ratio and shear modulus, respectively [41], and η is the accommodation factor further described below. Eqs. (15) and (16) are based on the work of Eshelby [56] for determining the strain energy of an inclusion which undergoes a shape change within an infinite matrix. The Olson and Cohen model does not consider the interaction energy between the contracted stacking fault and the partial dislocations. However, Müllner and Ferreira [55] modeled the strain field generated by two parallel partial dislocations and a contracted stacking fault using Somigliana dislocations to compute the total energy, including the interaction components. The interaction energy components involving the two Shockley partials were found to be small or vanishing compared to other components of the coherency strain energy. The Müllner and Ferreira model assumes that the coherency strain is volume preserving (i.e. $VS = 0$), which contrasts with our experimental measurements. Therefore, the method of Olson and Cohen was used to estimate the coherency strain energy in this study.

The orientation of the principal strain axes ε_{11} , ε_{22} and ε_{33} are assumed to remain unchanged by the transformation resulting in values of 0 for shear strains ε_{12} , ε_{23} and ε_{13} . The accommodation factor (η) is the ratio between the total energy per unit inclusion (i.e. martensite phase) volume embedded in the austenite phase to the energy per unit inclusion volume embedded in a hypothetical rigid matrix [29,56]. For pure dilatation, η is constant regardless of particle shape, and is built into Eq. (15). For shear strain, η may vary from 0 to 1, depending on particle shape and the strain state [56]. Following Refs. [29,31], η for a spherical inclusion, which is independent of strain state, is employed:

$$\eta = \frac{7 - 5\nu}{15(1 - \nu)} \quad (17)$$

Table 2 provides the lattice parameters of the fcc and ε_{hcp} -martensite phases obtained from the Rietveld refinement of XRD patterns from recrystallized specimens (for fcc) and those displayed in Fig. 7 from specimens deformed to failure (for hcp), with uncertainty representing equipment error. The XRD patterns in Fig. 7a–c are from the 22%, 25% and 28% Mn samples after deformation to failure at RT, -25 and -100 °C, respectively. The presence of strain-induced ε_{hcp} -martensite is confirmed for each condition, while the formation of strain-induced α -martensite is noted in the 22% and 25% Mn alloys.

A slight increase in the lattice parameters of the fcc phase with Mn content is observed, while no trend in the hcp lattice parameters can be deduced over the current range of Mn. Utilizing the lattice parameters from Table 2 in conjunction with the method reported by Olson and Cohen [29] yields ε_{11} , ε_{22} , ε_{33} , VS , E_{dil} , E_{sh} and $2\rho E_{\text{str}}$, as shown in Table 3. The uncertainties, calculated using a root sum square approach, are $\sim 25\%$ for ε_{11} , ε_{22} and ε_{33} and $\sim 43\%$ for VS . The uncertainties are $\sim 62\%$ and 79% for E_{dil}

Table 2
Lattice constants determined by XRD.

Alloy	fcc (Å)		ϵ_{hcp} -martensite (Å)	
	a_{fcc}	$c_{\text{fcc}} (2a_{\text{fcc}}/\sqrt{3})$	a_{hcp}	c_{hcp}
22%Mn	3.615 ± 0.001	4.175 ± 0.002	2.548 ± 0.003	4.153 ± 0.005
25%Mn	3.617 ± 0.001	4.177 ± 0.002	2.547 ± 0.003	4.151 ± 0.005
28%Mn	3.620 ± 0.001	4.180 ± 0.002	2.545 ± 0.003	4.152 ± 0.005

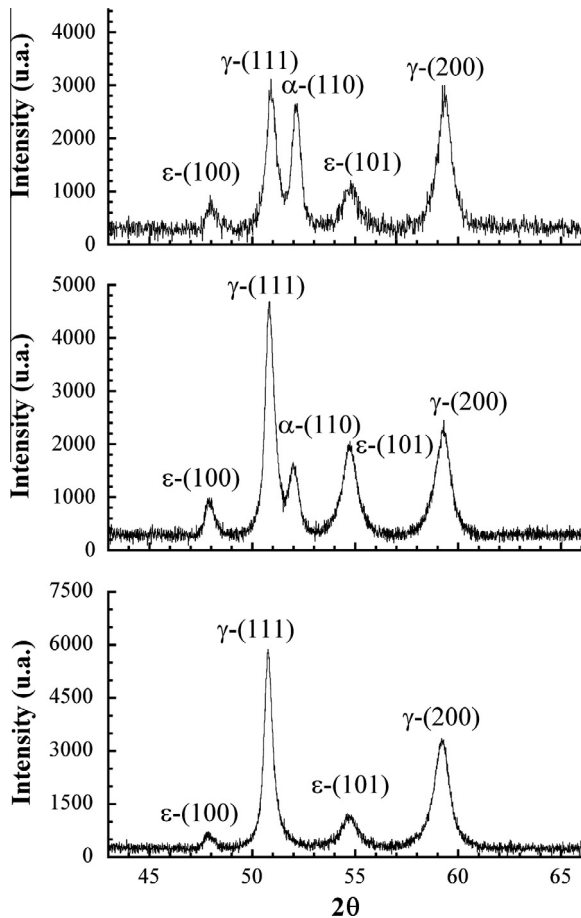


Fig. 7. XRD patterns for (top) an Fe–22Mn–3Al–3Si alloy deformed at room temperature, (middle) an Fe–25Mn–3Al–3Si alloy deformed at -25°C and (bottom) an Fe–28Mn–3Al–3Si alloy deformed at -100°C . All samples deformed to maximum uniform elongation. The peaks are labeled according to phase and reflection in Miller indices.

and E_{sh} . The value of E_{sh} is small compared to E_{dil} for the Fe–22/25/28Mn–3Al–3Si alloys, and consequently the uncertainty of $2\rho E_{str}$ is also $\sim 62\%$. The values of VS ranged from -0.011 to -0.018 (from -1.1% to -1.8%). Notwithstanding a substantial uncertainty in the calculation of the strain components, the experimental data suggest that contraction increases with Mn content. This is in line with the previous studies conducted on binary Fe–Mn steels [53,54]. The coherency strain energy (E_{str}) calculated by Olson and Cohen of 41.9 J mol^{-1} for an Fe–Cr–Ni steel is similar to the values calculated here (see Table 3). In addition, Müllner and Ferreira [55] calculated a value of 4.3 mJ m^{-2} for $2\rho E_{str}$ for a type 316 austenitic steel, which

is similar to the values calculated in the present work of 1.4 ± 0.87 , 2.3 ± 1.4 and $3.6 \pm 2.2\text{ mJ m}^{-2}$ for the Fe–22/25/28Mn–3Al–3Si alloys, respectively.

Fig. 8 shows the experimental (γ_{exp}) and ideal (γ_{∞}) SFE values. The dependence of γ_{exp} and γ_{∞} on Mn content above 24.7 wt.% is approximated as linear functions displayed in Fig. 8. The use of linear functions (rather than higher order polynomials) to describe the increase in SFE for Mn contents greater than 24.7 wt.% is consistent with other experimental SFE measurements which exhibit quasi-linear behavior from 25 to 35 wt.% Mn [32,57]. Quadratic polynomial functions of γ_{exp} and γ_{∞} as a function of Mn content (displayed in Fig. 8) were employed to approximate the SFE in the range of 22.2–24.7 wt.% Mn. The data indicate that a plateau of γ_{exp} and γ_{∞} occurs near 22 wt.% Mn, which is in good agreement with the experimentally observed minima of 22 wt.% Mn by Volosevich et al. [32] and between 20 and 25 wt.% (depending on purity of the Fe–Mn alloys) by Petrov et al. [57].

4.3. Thermodynamic modeling

To determine the interfacial energy from Eq. (4), a new thermodynamic model was developed to calculate $\Delta G_{Chem}^{fcc\rightarrow hcp}$ and $\Delta G_{Mag}^{fcc\rightarrow hcp}$ for the present Fe–Mn–Al–Si–C system. Existing thermodynamic models [3,12,26,27,30] for Fe–Mn-based steels were evaluated and deemed unsuitable for the present study for several reasons. The models of Saeed-Akbari et al. [27], Mosecker and Saeed-Akbari [12] and Nakano and Jacques [30] address the Fe–Mn–Al–C, Fe–Cr–Mn–N and Fe–Mn–C systems, respectively, but do not attempt to specifically address the influence of Si. Experimental studies on Fe–18Mn–0.6C–0/1.5Si [11] wt.% and Fe–31Mn– x Si–0.77C (at.%) alloys report decreases in the SFE with additions of Si. However, the model of Dumay et al. [26] shows that additions of Si up to ~ 4 wt.% increase the SFE of an Fe–22Mn–0.6C steel, disagreeing with the experimental results. The model of Curtze and Kuokkala [3] utilizes the same thermodynamic parameters as used by Dumay et al. [26] for both pure Si and its interaction with Fe. A thermodynamic model by Tian and Zhang [63] also predicts an increase in SFE for Fe–31Mn– x Si–0.77C ($x = \text{at.}\%$) alloys for Si additions up to 10.2 at.%. The more recent thermodynamic models of Nakano and Jacques [30] and Mosecker and Saeed-Akbari [12] show that the treatment of interstitial elements like C is enhanced by the use of a sublattice-type thermodynamic model. Finally, improved thermodynamic parameters for the Mn–C and Fe–Mn–C systems have recently been published by Djurovic et al. [64,65]. For the new model, the fcc and hcp phases were treated as randomly mixed substitutional solutions with two sublattices: substitutional and interstitial [12,30]:



with λ equal to 1 for fcc and 0.5 for hcp, assuming that interstitial elements do not occupy neighboring octahedral

Table 3
Parameters used in the calculation of $\sigma^{7/e}$ for Fe–Mn based alloys.

Parameter	Fe–22Mn– 3Al–3Si	Fe–25Mn– 3Al–3Si	Fe–28Mn– 3Al–3Si	Fe–16Mn	Fe–18Mn	Fe–20Mn	Fe–22Mn	Fe–25Mn	Fe–17.7Mn– 0.62C	Fe–17.7Mn– 0.59C–1.59Si	Fe–17.5Mn– 0.58C–1.54Al	Fe–18Mn– 0.6C	Fe–18Mn– 0.6C–1.5Al	Fe–18Mn– 0.6C–2.5Al
γ_{exp} (mJ m ⁻²) ^a	15 ± 3	21 ± 3	38.8 ± 5	26 ± 3.1	22 ± 2.6	18 ± 2.2	15 ± 1.8	27.5 ± 3.3	19.3 ± 2.5	13.8 ± 2.5	29.1	13 ± 3	30 ± 10	40.4
μ (GPa) ^b	72	72	72	69	69	69	69	69	71	72.5	70.1	71	70.1	70.1
ν ^b	0.24	0.24	0.24	0.23	0.23	0.23	0.23	0.23	0.23	0.24	0.24	0.23	0.24	0.24
e_{11} ^c	–0.0032	–0.0041	–0.0058	–0.0029	–0.0029	–0.0025	–0.0033	–0.0033						
e_{22} ^c	–0.0032	–0.0041	–0.0058	–0.0029	–0.0029	–0.0025	–0.0033	–0.0033						
e_{33} ^c	–0.0051	–0.0061	–0.0067	–0.0145	–0.0144	–0.0146	–0.0153	–0.0154						
VS ^c	–0.011	–0.014	–0.018	–0.020	–0.020	–0.019	–0.022	–0.022						
E_{dil} (J mol ⁻¹) ^d	24.1	38.3	61.1	69.2	69.4	65.1	81.7	83.4	71.4	74.4	72.0	71.4	72.0	72.0
E_{sh} (J mol ⁻¹) ^d	0.6	0.7	0.2	21.8	21.4	24.0	23.3	24.0	22.0	22.6	21.8	22.0	21.8	21.8
$2\rho E_{str}$ (mJ m ⁻²) ^d	1.4 ± 0.9	2.3 ± 1.4	3.6 ± 2.2	5.4 ± 0.5	5.4 ± 0.5	5.3 ± 0.5	6.2 ± 0.5	6.4 ± 0.5	5.5 ± 0.5	5.8 ± 0.5	5.6 ± 0.5	5.5 ± 0.5	5.6 ± 0.5	5.6
T_{Neel}^{fcc} (K) ^e	267	282	298	310	332	352	370	395	289	237	268	289	268	261
T_{Neel}^{hcp} (K) ^e	123	137	153	94	106	118	129	147	101	100	99	104	102	101
$2\rho\Delta G_{Chem}^{fcc\rightarrow hcp}$ (mJ m ⁻²) ^f	–6.7	–0.2	9.1	–48.4	–43.9	–38.8	–33.3	–24.2	–11.4	–13.2	1.0	–11.9	2.6	11.4
$2\rho\Delta G_{Mag}^{fcc\rightarrow hcp}$ (mJ m ⁻²) ^f	1.5	2.0	2.6	3.9	6.0	8.3	10.7	14.0	2.1	0.8	1.4	2.1	1.4	1.2
$\sigma^{7/e}$ (mJ m ⁻²) ^g	9.3 ± 1.6	8.6 ± 1.7	11.8 ± 2.7	32.5 ± 1.6	27.3 ± 1.3	21.6 ± 1.1	15.7 ± 0.9	15.7 ± 1.7	11.5 ± 1.3	10.3 ± 1.3	10.6 ± 1.3	8.6 ± 1.5	10.2 ± 5	11.1

^a Experimental SFEs taken from present work and [10,11,32]. The term γ_{exp} for the Fe–18Mn–0.6C–2.5Al alloy is calculated.

^b Shear modulus and Poisson's ratio taken from [10,11,32,41]. Assumed to be the same for Fe–18Mn–0.6C–1.5/2.5Al alloys.

^c Strain values obtained from lattice parameters determined in the present work and [53,54].

^d Strain energy terms are calculated using the strain values in accordance with Section 4.2 (strain values for Fe–18Mn grade used for Fe–18Mn–0.6C–0/1.5/2.5(Al/Si) alloys). Uncertainties for the Fe–22/25/28Mn–3Al–3Si and binary Fe–Mn alloys are based on the uncertainty of the lattice parameters and the standard deviation of $2\rho E_{str}$ (for Fe–16/18/20/22/25Mn alloys), respectively.

^e T_{Neel}^{fcc} is obtained from [30,58–60]. T_{Neel}^{hcp} is obtained from Eq. (28) [61].

^f Terms $2\rho\Delta G_{Chem}^{fcc\rightarrow hcp}$ and $2\rho\Delta G_{Mag}^{fcc\rightarrow hcp}$ were determined with the model developed in the present work.

^g Calculated interfacial energy in accordance with Eq. (4). Interfacial energy for Fe–18Mn–0.6C–2.5Al steel is calculated using Eq. (29).

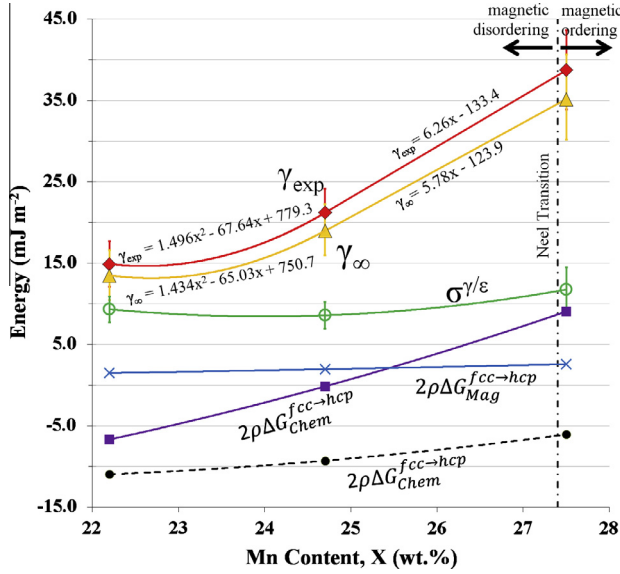


Fig. 8. Experimental SFE (γ_{exp}) and ideal SFE (γ_{∞}) values, with error bars representing the standard deviation of the measurements. Chemical ($2\rho\Delta G_{Chem}^{fcc\rightarrow hcp}$) and magnetic ($2\rho\Delta G_{Mag}^{fcc\rightarrow hcp}$) contributions to the difference in Gibbs free energy from the fcc to hcp phase transformation determined by the thermodynamic model (note: the values of $n\rho\Delta G_{Chem}^{fcc\rightarrow hcp}$ denoted by the dashed line were calculated using $L_{Fe,Mn:Va}^{hcp}$, as proposed by Djurovic et al. [65]). Interfacial parameters $\sigma^{\gamma/\epsilon}$ calculated from the experimental and theoretical data. All values are plotted as a function of Mn content. The dashed-dotted line indicates the Mn content at which the Néel transition occurs at 298 K for an Fe–X_{Mn}–2.7Al–2.9Si wt.% steel [60].

sites in the hcp structure [30,66]. The term Va stands for vacancy. The terms G_m^{hcp} and G_m^{fcc} are the molar Gibbs free energy of the individual phases, Φ (fcc or hcp) [12,30]:

$$G_m^{\Phi} = y_{Fe}^{\Phi} y_C^{\Phi} G_{Fe:C}^{\Phi} + y_{Fe}^{\Phi} y_{Va}^{\Phi} G_{Fe:Va}^{\Phi} + y_{Mn}^{\Phi} y_C^{\Phi} G_{Mn:C}^{\Phi} + y_{Mn}^{\Phi} y_{Va}^{\Phi} G_{Mn:Va}^{\Phi} + y_{Al}^{\Phi} \left(\frac{y_{Va}^{fcc} + y_{Va}^{hcp}}{2} \right) G_{Al:Va}^{\Phi} + y_{Si}^{\Phi} \left(\frac{y_{Va}^{fcc} + y_{Va}^{hcp}}{2} \right) G_{Si:Va}^{\Phi} + RT (y_{Fe}^{\Phi} \ln y_{Fe}^{\Phi} + y_{Mn}^{\Phi} \ln y_{Mn}^{\Phi} + y_{Al}^{\Phi} \ln y_{Al}^{\Phi} + y_{Si}^{\Phi} \ln y_{Si}^{\Phi}) + y_{Va}^{\Phi} \ln y_{Va}^{\Phi} + y_{C}^{\Phi} \ln y_{C}^{\Phi} + y_{ex} G_m^{\Phi} \quad (19)$$

In Eq. (19), R is the gas constant and T is the temperature in K. The site fractions of the individual elements, y_i in the substitutional lattice are calculated as:

$$y_i = \frac{x_i}{(1 - x_C)} \quad (20)$$

and for C in the interstitial lattice as:

$$y_C = \frac{x_C}{\lambda(1 - x_C)} \quad (21)$$

where x is the mole fraction of each element. Eq. (22) defines the correlation between the individual site fractions:

$$y_{Fe+Y_{Mn+Y_{Al+Y_{Si}}} = y_C + y_{Va} = 1 \quad (22)$$

The thermodynamic parameters $G_{i:Va}^{\Phi}$ and $G_{i:C}^{\Phi}$ in Eq. (19) are listed in Table 4. They represent the Gibbs energy of substitutional element i in phase Φ when all available interstitial sites are vacant (Va) or occupied by C, respectively.

The terms ${}^0G_{Al:C}^{\Phi}$ and ${}^0G_{Si:C}^{\Phi}$ were not included in Eq. (19) due to a lack of data for the hcp phase. In addition, average vacancy site fractions, $\left(\frac{y_{Va}^{hcp} + y_{Va}^{fcc}}{2} \right)$, were used for Si and Al and resulted in significantly better agreement with experimental results for steels with Si and C. The combined term $\Delta^0 G_{Si:Va}^{hcp\rightarrow fcc}$ replaces ${}^0G_{Si:Va}^{\Phi}$ and $RT y_{Si}^{\Phi} \ln y_{Si}^{\Phi}$ in the calculation of $\Delta G_{Chem}^{fcc\rightarrow hcp}$. The excess free energy is described as [30]:

$${}^{ex}G_m^{\Phi} = y_{Fe}^{\Phi} y_{Mn}^{\Phi} y_C^{\Phi} L_{Fe,Mn:C}^{\Phi} + y_{Fe}^{\Phi} y_{Mn}^{\Phi} y_{Va}^{\Phi} L_{Fe,Mn:Va}^{\Phi} + y_{Fe}^{\Phi} y_C^{\Phi} y_{Va}^{\Phi} L_{Fe:C:Va}^{\Phi} + y_{Mn}^{\Phi} y_C^{\Phi} y_{Va}^{\Phi} L_{Mn:C:Va}^{\Phi} + y_{Fe}^{\Phi} y_{Al}^{\Phi} \left(\frac{y_{Va}^{fcc} + y_{Va}^{hcp}}{2} \right) L_{Fe,Al:Va}^{\Phi} + y_{Mn}^{\Phi} y_{Al}^{\Phi} \left(\frac{y_{Va}^{fcc} + y_{Va}^{hcp}}{2} \right) L_{Mn,Al:Va}^{\Phi} + y_{Fe}^{\Phi} y_{Si}^{\Phi} \left(\frac{y_{Va}^{fcc} + y_{Va}^{hcp}}{2} \right) L_{Fe,Si:Va}^{\Phi} + y_{Mn}^{\Phi} y_{Si}^{\Phi} \left(\frac{y_{Va}^{fcc} + y_{Va}^{hcp}}{2} \right) L_{Mn,Si:Va}^{\Phi} \quad (23)$$

where $L_{i,j:C, Va}^{\Phi}$ is the interaction parameter for the elements in phase Φ , listed in Table 4. Parameters describing the interaction of Al and Si with C were not available for the hcp phase. Average vacancy site fractions were used for $L_{Fe,Al:Va}^{\Phi}$, $L_{Mn,Al:Va}^{\Phi}$, $L_{Fe,Si:Va}^{\Phi}$ and $L_{Mn,Si:Va}^{\Phi}$ to improve agreement with experimental SFE measurements of steels with interstitial C. For aluminium, the combined term $\Delta L_{Fe,Al:Va}^{hcp\rightarrow fcc}$ replaces $L_{Fe,Al:Va}^{\Phi}$ in Eq. (23) for the calculation of $G_{Chem}^{fcc\rightarrow hcp}$.

The magnetic contribution to the Gibbs energy of a phase is described by the model proposed by Inden [76] as modified by Hillert and Jarl [77]:

$$G_{Mag}^{\Phi} = RT \ln(\beta^{\Phi} + 1) f^{\Phi}(\tau^{\Phi}) \quad (24)$$

The term β^{Φ} is the magnetic moment of phase Φ divided by the Bohr magneton μ_b and given by Eqs. (25) and (26) [26].

$$\beta^{fcc} = 0.7x_{Fe} + 0.62x_{Mn} - 0.64x_{Fe}x_{Mn} - 4x_C \quad (25)$$

$$\beta^{hcp} = 0.62x_{Mn} - 4x_C \quad (26)$$

The term $f^{\Phi}(\tau^{\Phi})$ is a function of the scaled Néel temperature $\tau^{\Phi} = T/T_{Neel}^{\Phi}$, found elsewhere in the literature [3,27,67,76,77]. The Néel temperature for the fcc phase of Fe–Mn–Al–Si steels is described by King and Peters [60] as:

$$T_{Neel}^{fcc} = 199.5 + 6.0X_{Mn} - 10.4X_{Al} - 13X_{Si} \text{ (K)} \quad (27)$$

where X is the wt.% of the individual elements, and the hcp phase is described by Huang [61] as:

$$T_{Neel}^{hcp} = 580x_{Mn} \text{ (K)} \quad (28)$$

In Eq. (28), x_{Mn} is the molar fraction of Mn. If the lattice parameters of the materials are unknown, they may be estimated as a function of composition and temperature from equations listed in Ref. [27].

At room temperature (25 °C), the model predicts ($\Delta G_{Chem}^{fcc\rightarrow hcp} + \Delta G_{Mag}^{fcc\rightarrow hcp}$) to be -88 J mol^{-1} for the alloy with 22% Mn. This is a reasonable value, considering that thermal ϵ_{hcp} -martensite is not present yet mechanical ϵ_{hcp} -martensite forms upon deformation. Thermal ϵ_{hcp} -martensite typically

Table 4

Thermodynamic parameters for the Fe–Mn–Al–Si–C system from the literature used in this investigation unless otherwise stated.^a

	Ref.
<i>fcc Phase</i>	
${}^0G_{Fe:Va}^{fcc} = -236.7 + 132.416T - 24.664T \ln(T) - 0.00376T^2 - 5.893E^{-8}T^3 + 77358.5T^{-1}$	[67]
${}^0G_{Mn:Va}^{fcc} = -3439.3 + 131.884T - 24.5177T \ln(T) - 0.006T^2 + 69600T^{-1}$	[67]
${}^0G_{Fe:C}^{fcc} - {}^0G_{Fe:Va}^{fcc} - G_C^{Gra.} = 77,207 - 15.877T$	[68]
${}^0G_{Mn:C}^{fcc} = {}^0G_{Mn:Va}^{fcc} + G_C^{Gra.} + 13.659T$	[64]
${}^0G_{Al:Va}^{fcc} = -7976.15 + 137.093T - 24.367T \ln(T) - 1.8846E^{-3}T^2 - 0.87766E^{-6}T^3 + 74092T^{-1}$	[67]
$L_{Fe:Va,C}^{fcc} = -34,671$	[68]
$L_{Mn:Va,C}^{fcc} = -41,333$	[64]
$L_{Fe,Mn:C}^{fcc} = 20,082 - 11.6312T$	[65]
$L_{Fe,Mn:Va}^{fcc} = -7762 + 3.865T - 259(y_{Fe} - y_{Mn})$	[61]
$L_{Mn,Al:Va}^{fcc} = -84,517 + 29.999T + (-19,665 + 12.552T)(y_{Mn} - y_{Al})$	[69]
$L_{Fe,Si:Va}^{fcc} = -125248 + 41.116T - 142708(y_{Fe} - y_{Si}) + 89,907(y_{Fe} - y_{Si})^2$	[70]
$L_{Fe,Si:C}^{fcc} = 226100 - 34.25T - 202400(y_{Fe} - y_{Si})$ (not used)	[71]
$L_{Mn,Si:Va}^{fcc} = -88,555 + 2.94T - 7500(y_{Mn} - y_{Si})$	[72]
<i>hcp Phase</i>	
${}^0G_{Fe:Va}^{hcp} = -2480.08 + 136.725T - 24.664T \ln(T) - 0.00376T^2 - 5.893E^{-8}T^3 + 77358.5T^{-1}$	[67]
${}^0G_{Mn:Va}^{hcp} = -4439.3 + 133.007T - 24.5177T \ln(T) - 0.006T^2 + 69600T^{-1}$	[67]
${}^0G_{Fe:C}^{hcp} - {}^0G_{Fe:Va}^{hcp} - 0.5{}^0G_C^{Gra} = 52,905 - 11.9075T$	[30,68]
${}^0G_{Mn:C}^{hcp} = {}^0G_{Mn:Va}^{hcp} + 0.5{}^0G_C^{Gra} - 9000 - 1.0651T$	[64]
${}^0G_{Al:Va}^{hcp} = -2495.15 + 135.293T - 24.367T \ln(T) - 1.8846E^{-3}T^2 - 0.87766E^{-6}T^3 + 74092T^{-1}$	[67]
$L_{Fe:Va,C}^{hcp} = -17,335$	[30,68]
$L_{Mn:Va,C}^{hcp} = -5006$	[64]
$L_{Fe,Mn:C}^{hcp} = 21742 - 50.2703T - 32608(y_{Fe} - y_{Mn})$	[65]
$L_{Fe,Mn:Va}^{hcp} = -69.41 + 2.836T + ((-14271.46 + 13.884T)(y_{Fe} - y_{Mn}))$	[30]
$L_{Fe,Mn:Va}^{hcp} = -5748 + 3.865T + 273(y_{Fe} - y_{Mn})$	[65]
$L_{Mn,Al:Va}^{hcp} = -87027 + 17.154T + (-5774 + 8.786T)(y_{Mn} - y_{Al}) + (83931 - 47.279T)(y_{Mn} - y_{Al})^2$	[69]
$L_{Fe,Si:Va}^{hcp} = -106149 + 41.116T - 191658(y_{Fe} - y_{Si}) + 123574(y_{Fe} - y_{Si})^2$	[73]
$L_{Fe,Si:C}^{hcp} = \text{unavailable}$	
$L_{Mn,Si:Va}^{hcp} = -86775 + 2.94T - 7500(y_{Mn} - y_{Si})$	[74]
<i>Other</i>	
$\Delta G_{Si:Va}^{fcc \rightarrow hcp} = {}^0G_{Si:Va}^{hcp} - {}^0G_{Si:Va}^{fcc} = -560 - 8T$	[26]
$\Delta L_{Fe,Al:Va}^{hcp \rightarrow fcc} = L_{Fe,Al:Va}^{hcp} - L_{Fe,Al:Va}^{fcc} = 3326$	[75]
${}^0G_{Mn:Va}^{z} = -8115.28 + 130.059T - 23.4582T \ln(T) - 7.3476E^{-3}T^2 + 69827.1T^{-1}$	[67]
${}^0G_C^{Gra.} = -17368.441 + 170.73T - 24.3T \ln(T) - 4.723E^{-4}T^2 + 2562600T^{-1} - 2.643E^8T^{-2} + 1.2E^{10}T^{-3}$	[67]

^a Values in J mol⁻¹.

occurs when $(\Delta G_{Chem}^{fcc \rightarrow hcp} + \Delta G_{Mag}^{fcc \rightarrow hcp}) < -100 \text{ J mol}^{-1}$ [26], while mechanical ε_{hcp} -martensite is generally observed in Fe–Mn-based alloys where $(\Delta G_{Chem}^{fcc \rightarrow hcp} + \Delta G_{Mag}^{fcc \rightarrow hcp})$ is negative [12]. Thermal ε_{hcp} -martensite forms in a similar alloy (Fe–20Mn–3Al–3Si wt.%) with slightly less Mn content [24]. At 25% Mn, the term $(\Delta G_{Chem}^{fcc \rightarrow hcp} + \Delta G_{Mag}^{fcc \rightarrow hcp})$ is 31 J mol⁻¹ and the dominant secondary deformation mechanism is mechanical twinning [24]. These results are consistent with previous observations that Fe–Mn-based alloys with negative or positive values of $(\Delta G_{Chem}^{fcc \rightarrow hcp} + \Delta G_{Mag}^{fcc \rightarrow hcp})$ tend to exhibit strain-induced ε_{hcp} -martensite or mechanical twinning, respectively [12].

Fig. 8 displays the trends in $2\rho\Delta G_{Chem}^{fcc \rightarrow hcp}$, $2\rho\Delta G_{Mag}^{fcc \rightarrow hcp}$ and $\sigma^{7/6}$ as a function of Mn content. The chemical contribution, $2\rho\Delta G_{Chem}^{fcc \rightarrow hcp}$, increases with increasing Mn content from 22 to 28 wt.%, exhibiting a slight concave up trend, due to the stabilizing effect that Mn has on the fcc phase relative to the hcp. For the compositions analyzed, the increase in $2\rho\Delta G_{Chem}^{fcc \rightarrow hcp}$ is $\sim 3 \text{ mJ m}^{-2}$ per wt.% Mn, agreeing well with the experimentally observed SFE between 22 and 25 wt.% Mn. The calculation of $2\rho\Delta G_{Chem}^{fcc \rightarrow hcp}$ was also performed using the thermodynamic parameter $L_{Fe,Mn:Va}^{hcp}$ proposed by Djurovic et al. [65] (dashed line in Fig. 8). However, the calculated values of $2\rho\Delta G_{Chem}^{fcc \rightarrow hcp}$ using the

$L_{Fe,Mn:Va}^{hcp}$ proposed by Nakano and Jacques [30] agree more closely with the present experimental SFE measurements.

The hcp phase in each alloy is in the paramagnetic state at RT (the Néel temperatures are 123, 137 and 153 K for the 22%, 25% and 28% Mn alloys, respectively, based on Eq. (28)). Consequently, the influence of antiferromagnetic ordering on the hcp phase is insignificant at RT and $G_{Mag}^{hcp} \approx 0 \text{ J mol}^{-1}$ for the three alloys. The fcc phases of the alloys with 22% and 25% Mn are paramagnetic at RT (Néel temperatures are 267 and 282 K, respectively), while the fcc phase of the 28% Mn has a Néel temperature of $\sim 298 \text{ K}$ based on Eq. (27). The calculated values of G_{Mag}^{fcc} are -26 , -34 and -45 J mol^{-1} for the 22%, 25% and 28% Mn alloys, respectively. Therefore, $2\rho\Delta G_{Mag}^{fcc\rightarrow hcp}$ is small and increases from 1.5 to 2.6 mJ m^{-2} with increasing Mn content (see Fig. 8). For the present range of Mn content, the term $2\rho(\Delta G_{Chem}^{fcc\rightarrow hcp} + \Delta G_{Mag}^{fcc\rightarrow hcp})$ increases by 3.2 mJ m^{-2} per wt.% Mn, a slight increase compared to the rise due only to the chemical contribution. As Fe–Mn-based alloys are cooled to below T_{Neel}^{fcc} , the influence of antiferromagnetic ordering on properties such as electrical resistance and stiffness is gradual [59,60,78]. Accordingly, increasing T_{Neel}^{fcc} through room temperature by additions of Mn should produce only a gradual stabilization of the fcc phase due to magnetic ordering as the model currently predicts. However, $\Delta G_{Mag}^{fcc\rightarrow hcp}$ becomes large for alloys that are cooled to significantly below T_{Neel}^{fcc} [3] and partially counteracts the reduction in $\Delta G_{Chem}^{fcc\rightarrow hcp}$ with cooling. This explains why low deformation temperatures (-25 and $-100 \text{ }^\circ\text{C}$) are required to form sufficient quantities of ϵ_{hcp} -martensite in the 25% and 28% Mn alloys. The sensitivity of the SFE to temperature becomes less below T_{Neel}^{fcc} [30] due to the competing nature of $\Delta G_{Chem}^{fcc\rightarrow hcp}$ and $\Delta G_{Mag}^{fcc\rightarrow hcp}$. The Néel transition of most high-Mn TWIP and TRIP steels (especially those with Al and Si additions) is slightly below room temperature [59], save for the Fe–22Mn–0.6C wt.% grade [4]. Interestingly, stabilization of the fcc phase due to antiferromagnetic effects still occurs, owing to the gradual nature of this transition [4,59,60,78].

4.4. Interfacial energy calculation and behavior

In each alloy the interfacial energy is a major component of the SFE. The term $\sigma^{\gamma/\epsilon}$ is 9.3 ± 1.6 , 8.6 ± 1.7 and $11.8 \pm 2.7 \text{ mJ m}^{-2}$ for the Fe–22/25/28Mn–3Al–3Si alloys, respectively, from Eq. (4). The uncertainty of $\sigma^{\gamma/\epsilon}$ is obtained by dividing the root sum square of the uncertainties of γ_{exp} and $2\rho E_{str}$ by two. Using the same methodology, interfacial energy values were calculated for binary Fe–16/18/20/22/25Mn, Fe–18Mn–0.6C–0/1.5Al and Fe–18Mn–0.6C–0/1.5Si alloys from existing data in the literature. The calculation of $\sigma^{\gamma/\epsilon}$ used values of γ_{exp} reported by Volosevich et al. [32] (Fe–16/18/20/22/25Mn), Kim et al. [10] (Fe–18Mn–0.6–0/1.5Al) and Jeong et al. [11] (Fe–18Mn–

0.6C–0/1.5Al/Si). The values of $2\rho(\Delta G_{Chem}^{fcc\rightarrow hcp} + \Delta G_{Mag}^{fcc\rightarrow hcp})$ were determined with the thermodynamic model developed in Section 4.3. A summary of some of the parameters used in the calculation of $\sigma^{\gamma/\epsilon}$ are listed in Table 3. The interfacial energies of the Fe–18Mn–0.6C–0/1.5Al(Si) range from 8.6 to 11.5 mJ m^{-2} and are consistent with a range of 8.6– 11.8 mJ m^{-2} for the Fe–22/25/28Mn–3Al–3Si alloys. Interstitial C segregation may influence the experimental SFE measurements, but it is not accounted for in $\Delta G_{Chem}^{fcc\rightarrow hcp}$ or $\Delta G_{Mag}^{fcc\rightarrow hcp}$ (due to the assumption of homogeneous compositions). Therefore, Mosecker and Saeed-Akbari [12] proposed that the effects of interstitial segregation on γ_{exp} would be accounted for in the calculation of $\sigma^{\gamma/\epsilon}$. However, no substantial differences in the calculated values of $\sigma^{\gamma/\epsilon}$ are observed between the Fe–22/25/28Mn–3Al–3Si and Fe–18Mn–0.6C–0/1.5Al(Si) alloys, suggesting that the influence of segregation on the SFE measurements is minor. The calculated interfacial energies of the binary Fe–16/18/20/22/25Mn wt.% alloys range from 15.7 to 32.5 mJ m^{-2} and are noticeably higher than for the other alloys. The large difference is attributed to both the experimental procedure used to measure γ_{exp} [32] and the influence of $2\rho(\Delta G_{Chem}^{fcc\rightarrow hcp} + \Delta G_{Mag}^{fcc\rightarrow hcp})$ on the interfacial energy (which will be discussed in the following paragraph). The values of γ_{exp} [32] used in the interfacial calculation are higher than the actual values (as previously discussed) and therefore result in an overestimate of the interfacial energies for the binary Fe–Mn alloys. However, the trend in γ_{exp} vs. Mn reported by Volosevich et al. [32] is similar to other works [27,57,79] and provides confidence that the general trend

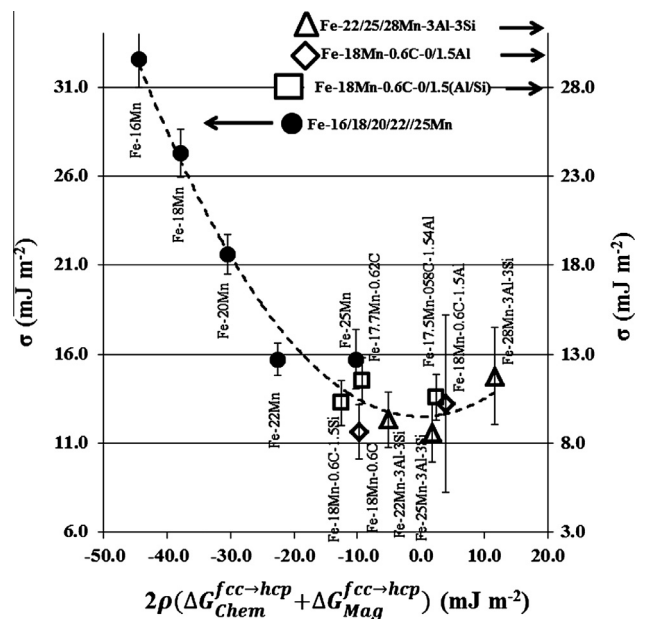


Fig. 9. Interfacial energy plotted as a function of $2\rho(\Delta G_{Chem}^{fcc\rightarrow hcp} + \Delta G_{Mag}^{fcc\rightarrow hcp})$ for Fe–22/25/28Mn–3Al–3Si, Fe–16/18/20/22/25Mn and Fe–18Mn–0.6C–0/1.5Al(Si) wt.% steels. The dashed line represents the best fit of the calculated interfacial energies.

in $\sigma^{\gamma/\varepsilon}$ (which is calculated from γ_{exp}) with changes in Mn content reflects the actual behavior.

In Fig. 9, the values of $\sigma^{\gamma/\varepsilon}$ are plotted as a function of $2\rho(\Delta G_{Chem}^{fcc\rightarrow hcp} + \Delta G_{Mag}^{fcc\rightarrow hcp})$ for all alloys. The dependence of $\sigma^{\gamma/\varepsilon}$ on $2\rho(\Delta G_{Chem}^{fcc\rightarrow hcp} + \Delta G_{Mag}^{fcc\rightarrow hcp})$ is consistent with parabolic behavior. In general, as $|2\rho(\Delta G_{Chem}^{fcc\rightarrow hcp} + \Delta G_{Mag}^{fcc\rightarrow hcp})|$ increases, the term $\sigma^{\gamma/\varepsilon}$ also increases, indicating that the interfacial energy is strongly related to $|\Delta G_{Chem}^{fcc\rightarrow hcp} + \Delta G_{Mag}^{fcc\rightarrow hcp}|$. Conversely, as $|\Delta G_{Chem}^{fcc\rightarrow hcp} + \Delta G_{Mag}^{fcc\rightarrow hcp}|$ approaches 0, where both fcc and hcp phases are equally favored, the resulting energy increase at the interface should be near a minimum, as is observed. Therefore, $\sigma^{\gamma/\varepsilon}$ can be approximated as a parabolic function of $2\rho(\Delta G_{Chem}^{fcc\rightarrow hcp} + \Delta G_{Mag}^{fcc\rightarrow hcp})$ with a minimum at $\sigma_{min}^{\gamma/\varepsilon}$:

$$\sigma^{\gamma/\varepsilon} = c(2\rho(\Delta G_{Chem}^{fcc\rightarrow hcp} + \Delta G_{Mag}^{fcc\rightarrow hcp}))^2 + \sigma_{min}^{\gamma/\varepsilon} \quad (\text{mJ m}^{-2}) \quad (29)$$

where c is a constant determined from fitting to experimental values. The term $\sigma_{min}^{\gamma/\varepsilon}$ is 9.5 mJ m^{-2} and results from the minimum fit for the Fe–22/25/28Mn–3Al–3Si and Fe–18Mn–0.6C–0/1.5(Al/Si) alloys. The constant c of 0.01 was determined by fitting a curve (dotted line in Fig. 9) to the trend in $\sigma^{\gamma/\varepsilon}$ as a function of $2\rho(\Delta G_{Chem}^{fcc\rightarrow hcp} + \Delta G_{Mag}^{fcc\rightarrow hcp})$ for the Fe–Mn–Al–Si, Fe–Mn–C–(Al/Si) and Fe–Mn alloys.

Non-monotonic behavior of $\sigma^{\gamma/\varepsilon}$ as a function of composition has been reported by other authors. Cotes et al. [31] showed that $\sigma^{\gamma/\varepsilon}$ varies as a function of Mn content for binary Fe–Mn alloys and can be approximated as an upward opening parabolic curve, with a minimum $\sigma^{\gamma/\varepsilon}$ occurring between 20 and 25 wt.% Mn. Mosecker and Saeed-Akbari [12] reported a similar behavior for the Fe–

Mn–Cr–N system, where $\sigma^{\gamma/\varepsilon}$ displays parabolic behavior with additions of nitrogen from 0.2 to 0.9 wt.%. These studies provide additional confidence that the underlying cause of the parabolic behavior is due to the relationship between $\sigma^{\gamma/\varepsilon}$ and $|\Delta G_{Chem}^{fcc\rightarrow hcp} + \Delta G_{Mag}^{fcc\rightarrow hcp}|$, as proposed in the present work.

4.5. Model validation

The thermodynamic model was used in conjunction with the empirical relationship for $\sigma^{\gamma/\varepsilon}$ to predict values of γ_{exp} and compare them with values from the literature. The calculated values of γ_{exp} (note: the calculated value includes $2\rho E_{str}$) are 16.7 and 28.9 mJ m^{-2} for Fe–18Mn–0.6C–0/1.5Al alloys and exhibit good agreement with experimental values of $13 \pm 3/30 \pm 10 \text{ mJ m}^{-2}$ [10] and $19.3 \pm 2.5/29.1 \pm 2.5 \text{ mJ m}^{-2}$ [11], respectively. Jung and De Cooman [80] reported mechanical twinning in an Fe–18Mn–0.6C–2.5Al alloy. The calculated values of γ_{exp} and γ_{∞} for this alloy are 40.4 and 34.8 mJ m^{-2} (see Table 3), which are in the SFE range for mechanical twinning as reported by Allain et al. [25] and in the present work. The calculated SFE values are reasonable for C contents up to 0.6 wt.%. In addition, the present SFE measurements for the Fe–22/25/28Mn–3Al–3Si alloys give confidence that the model is valid for Al additions up to 3 wt.%.

The range of Si for which the model is valid was tested by predicting T_0 temperatures (defined here as the average of the ε -martensite start (M_s) and austenite start (A_s) temperatures and corresponding to $(\Delta G_{Chem}^{fcc\rightarrow hcp} + \Delta G_{Mag}^{fcc\rightarrow hcp}) = 0$) of ternary Fe–Mn–Si alloys and comparing them to the experimental values reported by Cotes et al. [73,81]. The results of this comparison are reported in Table 5. Analysis of the data indicates that good agreement

Table 5
Experimental and calculated T_0 temperatures for Fe–Mn–Si ternary alloys.

	As (K) ^a	Ms (K) ^a	(As + Ms)/2 (K) ^a	Calculated (As + Ms)/2 (K)	% Diff ^b	T_{Neel}^{fcc} (K) ^c	T_{Neel}^{hcp} (K) ^c	$\Delta G_{Chem}^{fcc\rightarrow hcp}$ (J mol ⁻¹) ^d	$\Delta G_{Mag}^{fcc\rightarrow hcp}$ (J mol ⁻¹) ^d
Fe–17.5Mn–1.9Si	490	436	463	470	2	283	101	–6.0	6.0
Fe–17.4Mn–4.5Si	508	448	478	506	6	217	98	–1.1	1.1
Fe–19.5Mn–2.0Si	480	420	450	454	1	297	112	–8.6	8.6
Fe–22.2Mn–4.0Si	479	410	444.5	449	1	268	125	–5.1	5.1
Fe–24.2Mn–1.9Si	465	399	432	403	–7	336	140	–25.2	25.2
Fe–24.5Mn–4.2Si	465	396	430.5	421	–2	280	138	–8.1	8.1
Fe–26.5Mn–4.7Si	459	376	417.5	394	–6	282	149	–10.7	10.7
Fe–22.9Mn–6.1Si	470	402	436	455	4	222	127	–1.8	1.8
Fe–24.4Mn–6.4Si	464	379	421.5	433	3	226	135	–2.3	2.3
Fe–27.0Mn–5.9Si	453	363	408	387	–5	256	150	–6.8	6.8
Fe–19.9Mn–1.1Si	469	408	438.5	440	0	324	116	–15.2	15.2
Fe–22.1Mn–1.0Si	459	399	429	417	–3	344	129	–25.2	25.2
Fe–22.8Mn–2.8Si	468	401	434.5	429	–1	303	130	–11.4	11.4
Fe–28.4Mn–0.99Si	416	280	348	304	–13	390	165	–201.5	201.5
Fe–28.8Mn–4.74Si	443	351	397	353	–11	296	161	–20.9	20.9

^a From Refs. [73,81].

^b Difference between calculated and experimental T_0 temperatures.

^c T_{Neel}^{fcc} and T_{Neel}^{hcp} calculated from [58,61], respectively.

^d $\Delta G_{Chem}^{fcc\rightarrow hcp}$ and $\Delta G_{Mag}^{fcc\rightarrow hcp}$ calculated with present thermodynamic model.

is achieved between the experimental and calculated T_0 temperatures (within 7%) for Si additions up to ~6 wt.% in ternary Fe–Mn–Si alloys. At high Mn contents (28–29 wt.%), a greater deviation (~11–13%) is observed in the predicted vs. experimental T_0 temperatures. Therefore, the thermodynamic model is valid for a range of Mn content from 0 to 29 wt.% [30]. Jeong et al. [11] reported SFE measurements of 19.3 ± 2.5 and 13.8 ± 2.5 mJ m^{-2} for paramagnetic Fe–18Mn–0.6C and Fe–18Mn–0.6C–1.5Si wt.% alloys, respectively, finding that the addition of Si resulted in a decrease of 3.5 mJ m^{-2} per wt.%. The current thermodynamic model predicts values of γ_{exp} of 17.0 and 15.4 mJ m^{-2} for the same alloys, corresponding to a decrease in γ_{exp} of ~1 mJ m^{-2} per wt.% addition of Si. Tian and Zhang [62] experimentally measured a decrease in γ_{exp} of ~2.5 mJ m^{-2} per wt.% addition of Si in Fe–32Mn–0/4.6Si–0.2C alloys. Whereas the current model improves upon previous thermodynamic models which report an increase in SFE for small additions of Si, it would likely benefit from interaction parameters for Fe–Si–C for the hcp phase, an observation also shared by Jeong et al. [11]. Therefore, the model should be limited to Si concentrations of up to ~1.5 wt.% for alloys with C contents of ~0.6 wt.%.

The values of $2\rho\Delta G_{Mag}^{fcc\rightarrow hcp}$, $2\rho\Delta G_{Chem}^{fcc\rightarrow hcp}$, $2\rho E_{str}$ and $\sigma^{\gamma/\epsilon}$ determined in this work (Fig. 8) provide a greater understanding of the physical phenomena behind the SFE evolution in Fe–Mn-based steels. Of particular interest is the interfacial energy parameter, which is typically the largest parameter to contribute to the SFE in these materials at RT. This parameter exhibits a minimum near the point at which the Gibbs free energies of the fcc and hcp phases are equal and increases when the absolute value of the term $2\rho(\Delta G_{Chem}^{fcc\rightarrow hcp} + \Delta G_{Mag}^{fcc\rightarrow hcp})$ becomes larger (see Fig. 9). In the present Fe–22/25/28Mn–3Al–3Si steels, for Mn contents greater than ~23.5 wt.%, the terms $\sigma^{\gamma/\epsilon}$, $2\rho\Delta G_{Mag}^{fcc\rightarrow hcp}$ and $2\rho\Delta G_{Chem}^{fcc\rightarrow hcp}$ are all positive and increase with Mn content, resulting in a sharp rise of the SFE. However, for decreasing Mn content below ~23.5 wt.%, only the interfacial energy increases. This results in a much flatter SFE curve or minimum in this region, observed in both experimental [32,33] and theoretical studies [27,30], before a subsequent increase in SFE occurs with further reductions in Mn content.

5. Summary and conclusions

In this study the effect of Mn content on the SFE was investigated by measuring dissociation widths of partial dislocation pairs in three Fe–22/25/28Mn–3Al–3Si wt.% alloys, yielding SFE values of 15 ± 3 , 21 ± 3 and 39 ± 5 mJ m^{-2} , respectively. The strain energy associated with the contraction in molar volume during the austenite to ϵ_{hcp} -martensite transformations was determined to be ~1–4 mJ m^{-2} , resulting in ideal SFE values of 14 ± 3 , 19 ± 3 and 35 ± 5 mJ m^{-2} .

A new thermodynamic model for the Fe–Mn–Al–Si–C system is proposed which determines the chemical and magnetic components of the difference in Gibbs free energy of the fcc and hcp phases. The new model provides improved agreement with experimental observations of the influence of Si on the SFE in Fe–Mn-based alloys. The ideal SFE values were used in conjunction with the thermodynamic phase data to determine the fcc/hcp interfacial energies of the three Fe–Mn–(Al–Si) steels, as well as Fe–Mn and Fe–Mn–C–Al/Si alloys for which experimental SFE data are available in the literature. Calculations of the fcc/hcp interfacial energy parameter yielded values ranging from 8.6 to 11.8 mJ m^{-2} for the Fe–22/25/28Mn–3Al–3Si and Fe–18Mn–0.6C–0/1.5(Al/Si) wt.% TRIP and TWIP alloys. The interfacial energy of the binary Fe–Mn alloys ranged from 15.7 to 32.5 mJ m^{-2} . The present work shows a strong correlation between the value of the interfacial energy of Fe–Mn–(Al, Si, C) steels and the difference in free energy of the fcc and hcp phases. An empirical relationship to describe the interfacial energy is proposed to improve the accuracy of SFE calculations. The combined thermodynamic model and empirical relationship exhibits good agreement with the present SFE measurements and those in the literature, making it a useful tool for the design of high-Mn TRIP/TWIP steels. A follow-on study will investigate the relationship between SFE value, microstructural evolution and mechanical properties.

Acknowledgements

This work is sponsored by the National Science Foundation Division of Materials Research, USA, under Grant DMR0805295 and by the Comisión Interministerial de Ciencia y Tecnología (CICYT), Spain, under Grant MAT2012-39124. We would like to thank Dr. Bengt Hallstedt, Materials Chemistry, RWTH Aachen University, for technical discussions.

References

- [1] Grässel O, Krüger L, Frommeyer G, Meyer LW. *Int J Plast* 2000;16:1391.
- [2] Barbier D, Gey N, Allain S, Bozzolo N, Humbert M. *Mater Sci Eng A* 2009;500:196.
- [3] Curtze S, Kuokkala VT. *Acta Mater* 2010;58:5129.
- [4] Bouaziz O, Allain S, Scott CP, Cugy P, Barbier D. *Curr Opin Solid State Mater Sci* 2011;15:141.
- [5] Vercammen S. Processing and tensile behaviour of TWIP steels, microstructural and textural analysis. Leuven: Katholieke Universiteit Leuven; 2004.
- [6] De Cooman BC, Kwon O, Chin KG. *J Mater Sci Technol* 2012;28:513.
- [7] Saeed-Akbari A, Mosecker L, Schwedt A, Bleck W. *Metall Mater Trans A* 2012;43:1688.
- [8] Saeed-Akbari A, Schwedt A, Bleck W. *Scripta Mater* 2012;66:1024.
- [9] Gutierrez-Urrutia I, Raabe D. *Acta Mater* 2011;59:6449.
- [10] Kim J, Lee SJ, De Cooman BC. *Scripta Mater* 2011;65:363.
- [11] Jeong K, Jin JE, Jung YS, Kang S, Lee YK. *Acta Mater* 2013;61:3399.
- [12] Mosecker L, Saeed-Akbari A. *Sci Technol Adv Mater* 2013;14:1.

- [13] Gutierrez-Urrutia I, Raabe D. *Acta Mater* 2012;60:5791.
- [14] Steinmetz DR, Jäpel T, Wietbrock B, Eisenlohr P, Gutierrez-Urrutia I, Saeed-Akbari A, et al. *Acta Mater* 2013;61:494.
- [15] Gutierrez-Urrutia I, Zaefferer S, Raabe D. *Mater Sci Eng A* 2010;527:3552.
- [16] Remy L. *Acta Metall* 1978;26:443.
- [17] Bouaziz O, Guelton. *Mater Sci Eng A* 2001;319–321:246.
- [18] Allain S, Chateau J-P, Bouaziz O. *Mater Sci Eng A* 2004;387–389:143.
- [19] Bouaziz O, Allain S, Scott C. *Scripta Mater* 2008;58:484.
- [20] Barbier D, Favier V, Bolle B. *Mater Sci Eng A* 2012;540:212.
- [21] Dancette S, Delannay L, Renard K, Melchior MA, Jacques PJ. *Acta Mater* 2012;60:2135.
- [22] Kim J, Estrin Y, Beladi H, Timokhina I, Chin KG, Kim SK, et al. *Metall Mater Trans* 2012;43:479.
- [23] Shun T, Wan CM, Byrne JG. *Acta Metall* 1992;40:3407.
- [24] Grässel O, Frommeyer G, Derder C, Hofmann H. *J Phys IV* 1997;7:C5-383.
- [25] Allain S, Chateau JP, Bouaziz O, Migot S, Guelton N. *Mater Sci Eng A* 2004;387–389:158.
- [26] Dumay A, Chateau JP, Allain S, Migot S, Bouaziz O. *Mater Sci Eng A* 2008;483–484:184.
- [27] Saeed-Akbari A, Inlaur J, Prah U, Bleck W. *Metall Mater Trans A* 2009;40:3076.
- [28] Wittig JE, Pozuelo M, Jimenez JA, Frommeyer G. *Steel Res Int* 2009;80:66.
- [29] Olson GB, Cohen M. *Metall Trans A* 1976;78:1897.
- [30] Nakano J, Jacques PJ. *Calphad* 2010;34:167.
- [31] Cotes SM, Fernandez Guillermet A, Sade M. *Metall Mater Trans A* 2004;35:83.
- [32] Volosevich PY, Gridnev VN, Petrov YN. *Phys Metals Metallogr* 1976;42:126.
- [33] Volosevich PY, Gridnev VN, Petrov YN. *Phys Metals Metallogr* 1975;40:90.
- [34] Bampton CC, Jones IP, Loretto MH. *Acta Metall* 1978;26:39.
- [35] Pierce DT, Bentley J, Jimenez JA, Wittig JE. *Scripta Mater* 2012;66:753.
- [36] Idrissi H, Renard K, Ryelandt L, Schryvers D, Jacques PJ. *Acta Mater* 2010;58:2464.
- [37] Hirth JP, Lothe J. *Theory of dislocations*. 2nd ed. New York: Wiley; 1982.
- [38] Gebhardt T, Music D, Kossmann D, Ekholm M, Abrikosov IA, Vitos L, et al. *Acta Mater* 2011;59:3145.
- [39] Reeh S, Music D, Gebhardt T, Kasprzak M, Jäpel T, Zaefferer S, et al. *Acta Mater* 2012;60:6025.
- [40] Friak M, Hickel T, Körmann F, Udyansky A, Dick A, Von Pezold J, et al. *Steel Res Int* 2011;82:86.
- [41] Pierce DT, Nowag K, Montagne A, Jiménez JA, Wittig JE, Ghisleni R. *Mater Sci Eng A* 2013;578:134.
- [42] Cockayne DJH. *Z Naturforsch* 1972;27a:452.
- [43] Cockayne DJH. *J Phys* 1974;35:141.
- [44] Williams DB, Carter CB. *Transmission electron microscopy, a text book for materials science*. 2nd ed. New York: Springer; 2009.
- [45] Edington JW. *Practical electron microscopy in materials science*. Herndon: Tech Books; 1976.
- [46] Aerts E, Delavignette P, Siems R, Amelinckx S. *J Appl Phys* 1962;33:3078.
- [47] Teutonico LJ. *Philos Mag* 1966;15:959.
- [48] Eshelby JD, Read WT, Shockley W. *Acta Metall* 1953;1:251.
- [49] Foreman AJE. *Acta Metall* 1955;3:322.
- [50] Teutonico LJ. *Acta Metall* 1963;11:1283.
- [51] Cockayne DJH, Vitek V. *Phys Stat Sol B* 1974;65:751.
- [52] Brooks JW, Lorretto MH, Smallman RE. *Acta Metall* 1979;27:1839.
- [53] Marinelli P, Baruj A, Fernandez Guillermet A, Sade M. *Z Metallkd* 2001;91:957.
- [54] Marinelli P, Baruj A, Fernandez Guillermet A, Sade M. *Z Metallkd* 2001;92:489.
- [55] Müllner P, Ferreira PJ. *Philos Mag Lett* 1996;73:289.
- [56] Eshelby JD. *Proc Roy Soc A* 1957;241:376.
- [57] Petrov YN, Volynova TF, Yakubtsov IA, Medov IB, Mnasin VM. *Phys Metals Metallogr* 1989;68:169.
- [58] Jin JE, Jung M, Lee CY, Jeong J, Lee YK. *Met Mater Int* 2012;18:419.
- [59] Jung I, Lee S-J, De Cooman BC. *Scripta Mater* 2012;66:729.
- [60] King HW, Peters MA. *Can Metall Quart* 1997;36:137.
- [61] Huang W. *Calphad* 1989;13:243.
- [62] Tian X, Zhang Y. *Mater Sci Eng A* 2009;516:73.
- [63] Tian X, Zhang Y. *Mater Sci Eng A* 2009;516:78.
- [64] Djurovic D, Hallstedt B, Von Appen J, Dronskowski R. *Calphad* 2010;34:279.
- [65] Djurovic D, Hallstedt B, Von Appen J, Dronskowski R. *Calphad* 2011;35:479.
- [66] Frisk K. *Calphad* 1993;17:335.
- [67] Dinsdale AT. *Calphad* 1991;15:317.
- [68] Gustafson P. *Scand J Metall* 1985;14:259.
- [69] Shukla A, Pelton AD. *J Phase Equilib Diffus* 2009;30:28.
- [70] LaCaze J, Sundman B. *Metall Trans A* 1991;22:2211.
- [71] Miettinen J. *Calphad* 1998;22:231.
- [72] Li L, Hsu TY. *Calphad* 1997;21:443.
- [73] Cotes S, Fernandez Guillermet A, Sade M. *J Alloys Compd* 1998;280:168.
- [74] Forsberg A, Agren J. *J Phase Equilib* 1993;14:354.
- [75] Yang WS, Wan CM. *J Mater Sci* 1990;25:1821.
- [76] Inden G. *Phys B* 1981;103:82.
- [77] Hillert M, Jarl M. *Calphad* 1978;2:227.
- [78] Cankurtaran M, Saunders GA, Ray P, Wang Q. *Phys Rev B* 1993;47:3161.
- [79] Schumann H. *Kristall und Technik* 1974;9:1141.
- [80] Jung I-C, De Cooman BC. *Acta Mater* 2013;61:6724.
- [81] Cotes S, Fernandez Guillermet A, Sade M. *J Alloys Compd* 1998;278:231.